

## Chapter 3

### Geometry and Test Matrix

The work presented in this thesis focused on two different parts of a turbine blade, the tip region and the platform, also known as the hub. The research undertaken for each geometry involved a comprehensive study of various cooling techniques and flow phenomena within a turbine cascade to obtain a better understanding of the underlying physics. Both the tip and platform models proved to be extremely interesting and challenging. The unique features and characteristics of the geometry and cooling mechanisms explored will be discussed in the following pages along with a general discussion of the work undertaken during the study.

Experimental testing and computations were performed on both platform and tip cross-sectional geometries from the first stage turbine of an aero engine, but at the time this thesis was completed only the experimental data (Couch, 2003) from the tip testing was available for comparisons with the CFD predictions. Turbine blades typically vary continuously in the radial direction from the platform to the tip geometry, as seen on an actual blade in Figure 3.1 a-c. The tests and geometry presented in this study were performed on two-dimensional, scaled models of the respective geometric cross-sections at the tip and hub. This constant spanwise geometry was necessary because the experimental, linear cascade wind tunnel does not have the capability to match the varying inlet conditions required for a true turbine blade. A full discussion of blade scaling when moving from the engine to an experimental/computational domain is presented in Section 3.1.

The first study involved the investigation of flow through a tip gap. As a turbine blade rotates there is a gap between the outer casing, typically referred to as the shroud or blade outer air seal (BOAS) and the blade. This region more so than others is prone to failure. Factors for this failure stem from the small amount of material at the tip edge, the difficulty in providing adequate coolant to the region and the hot mainstream gas that is drawn into the tip gap. A series of computational tests were performed to analyze the

flow and heat transfer phenomena within and around the tip region with a full discussion to follow in Section 3.2.

The second major investigation involved the study of the platform to examine various cooling methods at the base of the turbine blade. As with the tip gap, the turbine endwall is exposed to extremely hot gases from the combustor and must be cooled in order to prevent burn-out and oxidation. In many instances, the combustor gases experience large temperature fluctuations that can create stress fractures from both mechanical and thermal loading. A detailed discussion of the platform test matrix including all of the simulations performed and each of the respective geometries will be discussed in Section 3.3 with additional details about the full flow field and thermal analysis presented throughout the text.

### **3.1 Blade Scaling**

To begin any discussion about turbine blades one must first be familiar with some of the basic geometric terminology used within the gas turbine community. Figure 3.2a-b shows some of these basic features that will be referenced throughout the text for the tip and platform geometries, respectively. Included in this figure is the pitch,  $P$ , measuring the blade spacing (Y-axis), the axial chord,  $B_x$ , measuring the axial distance (X-axis) through the blade passage from leading edge to trailing edge and the true chord,  $C$ , which travels from the stagnation point along the leading edge to the trailing edge with a straight line. Another important feature is the entrance angle,  $\theta$ , and the blade angle,  $\phi$ . Theta defines the direction of the incoming flow from the upstream stator vanes and is measured from the horizontal while  $\phi$  defines the orientation of the blade within the cascade and is also measured from the horizontal. Not shown in the figure is the span,  $S$ , which is the length of the blade in the Z-direction. Also worth noting is the coordinate system, where  $X, Y, Z$  and  $U, V, W$  are the global coordinates for position and velocity with the origin located at the blade stagnation point while local coordinates and local velocity are defined by  $x, y, z$  and  $u, v, w$ .

Before any experimental or computational testing could begin, it was important to establish a scaling factor for the desired tip and platform tests. Scaling of the blade provides many benefits, but the primary motivation is the ability to obtain better experimental temperature resolution using a scaled blade. All experimental work was conducted in a low-speed facility, which will be discussed in some detail in Chapter 7. This meant that it would be nearly impossible to create true engine-like conditions since turbine inlet temperatures normally exceed 3000° F. To obtain data that could be useful and applicable to the operation of a gas turbine required the matching of non-dimensional factors such as the Reynolds number. While it may be impossible to match turbine Mach numbers and temperatures it is certainly possible to match an engine Reynolds numbers. Calculations by Pratt and Whitney, Blair [2002] showed that by matching the engine Reynolds number during experiments the blowing ratio would be off by a factor of 1.79 as shown in Appendix A.

Blade scaling started by defining the engine Reynolds number along the tip and platform. Knowing the engine Reynolds number at these locations then allows for a relation between the engine and the test rig as shown in equation 3.1 where the subscript e represents engine conditions and r represents the test rig. In the equation,  $X_e$  is set as one and a solution is obtained for  $X_r$  which becomes the scaling factor.

$$Re_e = \frac{\rho_e U_e X_e}{\mu_e} = \frac{\rho_r U_r X_r}{\mu_r} = Re_r \quad (3-1)$$

With the Virginia Tech wind-tunnel operating around room temperature this fixes the two properties of air used in the Reynolds number calculations meaning the only other values that may vary are the reference length and flow velocity. The wind-tunnel has a maximum velocity of approximately 15 m/s for the geometry being considered, which further limits the scaling. For this scaling exercise the axial chord was chosen as the reference length. These requirements quickly limit the scale factor that can be chosen.

Another consideration when determining a scaling factor is the ability to achieve periodic flow conditions. The ability of experiments and computations to achieve periodic conditions, whereby there will be equal and similar flow conditions around several turbine blades is critical to obtaining successful results. To experimentally achieve periodic conditions several flow passages are required making it necessary to

have a least two pitches (three blades) within the facility. The flow through these passages may be controlled by several methods, which include the use of tail-boards and flexible walls, all of which is located downstream of the test section and is discussed in detail by Couch [2003], Christophel [2003] and Ranson [2004]. Computationally, periodicity is obtained by the application of a periodic boundary condition along the walls in the pitchwise direction when modeling a single turbine passage.

Another critical parameter to match from engine conditions is the pressure distribution around the blade. This was extremely important for the tip geometry as pressure has been determined to be the major factor driving flow from the pressure side to the suction side of the blade with the presence of a tip gap. Any pressure deviation from engine conditions could provide misleading results. To obtain an accurate pressure distribution at low speed conditions both the tip and platform blade cross-sections were redesigned for low speed testing. Work by Praisner [2002] of Pratt and Whitney on both the high-speed and low-speed tip cross-sections is shown in Figure 3.3 with the respective high and low speed blade designs.

The geometric and wind-tunnel constraints discussed above established a scaling factor of 12X engine geometry for tip testing. This equated to a Reynolds number of  $2.1 \times 10^5$  (based on axial chord,  $B_x$ ) and two passages in the experimental facility. The platform geometry required the use of three passages and an 11X scale in order to match half of the engine Reynolds number,  $3.0 \times 10^5$ . Additional flow calculations can be seen in Appendix A while a comprehensive presentation with more detailed drawings and specifications of both the tip and platform will be presented in the following sections and chapters.

### **3.2 Turbine Blade Tip Simulations: Test Matrix and Geometry**

To maintain a clearance between the blade tip and outer shroud, there is a tolerance gap that is specified in most turbine designs. This gap distance can change during the course of operation as a result of a range of temperatures within the turbine. Unfortunately, this gap provides a path for flow leakage across the blade tip reducing

aerodynamic efficiency and blade life. The tip gap flow is driven by a pressure differential from the pressure side to the suction side of the blade, but is limited by viscous forces as the fluid comes into contact with the walls of the gap. This leakage flow is normally hot gas that has migrated up the pressure side of the blade. In a typical engine the extremely high temperatures coupled with the highly turbulent flow in the tip region cause heat transfer to be unusually high in a region that is difficult to cool.

This study investigates several methods of turbine blade cooling, which include the use of a recessed cavity within the tip fed by coolant air from two dirt purge holes and the use of small air ducts located throughout the tip called microcircuits. The location of the dirt purge holes and microcircuit holes are shown in tip cross-section of Figure 3.4. The dirt purge holes are located on the surface of the tip near the leading edge and exhaust cool air normal to the blade while the microcircuit exit holes are located throughout the tip region, internally circulating cool air throughout the tip region before exhausting the air on the pressure side of the blade. It is hoped that the microcircuit can provide extensive internal and external cooling. In addition to studying cooling effectiveness, several baseline cases without coolant are studied to examine the variation in the flow field between tests with and without coolant.

To some extent the dirt purge cavity resembles the geometry seen in a squealer tip, but this cavity does not extend over the entire tip region. Most blades have these dirt purge holes and cavity as they are necessary during the blade casting process, but their effects on flow and heat transfer up to this point have largely been ignored. The dirt purge extends only over a small area in the front portion of the blade as shown in Figure 3.5. The figure is oriented looking from the pressure side towards the suction side of the blade with the pressure side sheathing removed to provide a view of the plenum and dirt purge features. The two ducts of the dirt purge measure 0.010m in diameter and feed a dirt purge cavity that measures  $7.0d$  by  $2.9d$ , where  $d$  is the diameter of the dirt purge holes. The depth of the cavity is  $0.6d$  and is located approximately  $4.0d$  from the blade leading edge. The two purge holes are  $2.9d$  in length and  $3.5d$  apart with a large plenum located inside the blade supplying the coolant air.

The dirt purge has several functions that include the following: it allows for dirt ingested by the compressor to be exhausted into the turbine without clogging film cooling

holes, it provides coolant to the front portion of the blade tip and it is a necessary part of the blade casting process. Rotational forces help to insure that debris ingested at the inlet is exhausted through the dirt purge holes that are somewhat larger than most film cooling holes. The dirt purge cavity is present to insure that during blade rubbing the purge holes remain open.

The microcircuit was the other component used to provide coolant to the tip region and is being considered for use in future blade designs as the concept is relatively new and untested. Unlike dirt purge cooling, which only provides coolant to the leading edge region, the microcircuit has the ability to cool most of the tip. The microcircuit design is composed of tiny air ducts located throughout the tip region and is fed by a large plenum inside the blade that is also used for dirt purge cooling. Each microcircuit duct varies internally in both size and shape to provide internal convective cooling throughout the tip region as shown in Figure 3.6a-c. Each of the respective images shows a slightly different view of this unique design ranging from a top view in Figure 3.6a to two isometric views in Figure 3.6b-c showing the upper and lower profiles, respectively. The microcircuit itself was divided into two separate parts consisting of a circuit in the leading edge and another in the mid-chord and aft section of the blade. Coolant air enters the circuit through ten supply ducts and is directed out of the microcircuit through sixteen exhaust holes located primarily on the pressure side of the blade. Each of those exhaust holes, including those of the dirt purge was given a number one through eighteen in order to identify the flow duct throughout the remainder of this text. The number and its associated hole may be seen in Figure 3.7. With tip leakage flow traveling from the pressure side of the blade to the suction side and the microcircuit air being injected along the pressure side of the blade, the degree to which the coolant air blocks the leakage flow is studied as well as external cooling effects along the tip.

Figure 3.8a-c shows the microcircuit and dirt purge positioned inside a blade with part of the pressure side sheathing removed. Important to notice in these pictures is the large extent over which the microcircuit spans. It is hoped that this new and innovative technology results in increased cooling through both added internal and external cooling. Looking at Figure 3.8c one can see that the microcircuit and surface of the blade tip are very close, allowing for significant heat to be conducted away from the tip before the

coolant air is exhausted into the mainstream. While internal cooling is a significant part of the microcircuit design this study is focused on examining the external cooling effects of the microcircuit with additional experimental work looking at internal cooling.

Table 3.1 shows some important geometric features of the tip study. Included in this table are measurements of the pitch, chord, axial chord, inlet flow angle, blade rotation angle, inlet Reynolds number, the temperature difference between the mainstream and coolant flows and the tip gap heights. These values were used in conjunction with the blade profile to construct computational models. Both the meshing and computational methodologies will be discussed in detail throughout Chapter 4 as general geometry and testing information is presented within this chapter.

With two different cooling methods to explore (microcircuit and dirt purge), work began to establish an array of tests that would provide information about a variety of features including: the tip leakage with and without coolant, variations in secondary flows and thermal field patterns, and temperature distributions along walls. A complete test matrix from the tip study is shown in Table 3.2. The test matrix consists of a detailed computational study of four different geometries to examine both flow and cooling characteristics when exposed to two tip gap sizes and various blowing ratios where applicable.

The four geometries considered for the tip tests are shown in Figure 3.9a-d and include a flat blade tip with no coolant, a blade tip with a dirt purge cavity and no cooling, a blade tip with a dirt purge cavity and holes to deliver coolant, and finally a blade with microcircuit and dirt purge cooling. The first two geometries served as baseline cases and were run without cooling. These models were used for comparing flow patterns to those instances where there was tip blowing. Each geometry was tested at a large tip gap measuring 1.63% of the span ( $H = 0.009\text{m}$  at 12x scale) and a small tip gap measuring 0.54% of the span ( $h = 0.003\text{m}$  at 12x scale). The latter two geometries (Figure 3.9c-d), consisting of a dirt purge with cooling and a microcircuit and dirt purge with cooling involved the exploration of multiple blowing ratios. Four blowing ratios were computed for the microcircuit geometry (0.5%, 1.0%, 1.5%, 2.0% of the overall mass flow through one passage) while a total of five blowing ratios were explored for the dirt purge tests (0.05%, 0.10%, 0.19%, 0.29%, 0.38% of the overall mass flow through

one passage). Baseline microcircuit flowrates were calculated by Blair [2002] (Appendix A) of 1.0% and 1.5% with additional blowing ratios of 0.5% and 2.0% added for completeness. Flowrates for the dirt purge cooling tests were calculated by first examining the combined microcircuit and dirt purge tests and determining the flowrates through each dirt purge hole. It was found that cases of 1.0% and 1.5% cooling through the microcircuit and dirt purge resulted in 0.19% and 0.29% of that coolant going to the dirt purge, respectively. Dirt purge cooling levels of 0.05%, 0.10% and 0.38% were also added. In total, 22 different tip scenarios were explored.

Averaged mass flux, momentum flux and velocity ratios are presented in Table 3.3 for each of the nine different flowrates that were run considered. These were calculated by taking the total coolant mass flowrate and backing out the average velocity using the coolant density and total cross-sectional area at the coolant discharge locations. The mass flux ratio, momentum flux ratio and velocity ratio are defined by the following equations.

$$M = \frac{\rho_c U_c}{\rho_\infty U_\infty} \quad (3-2)$$

$$I = \frac{\rho_c U_c^2}{\rho_\infty U_\infty^2} \quad (3-3)$$

$$VR = \frac{U_c}{U_\infty} \quad (3-4)$$

Figure 3.10 depicts each microcircuit and dirt purge hole with its position on a non-dimensionalized blade. In this figure the vertical axis is non-dimensionalized by the blade pitch,  $P$  while the horizontal axis uses the axial chord,  $B_x$ . The stagnation point is located at the origin with each microcircuit duct (shown in red) positioned relative to this point.

The five microcircuit exhaust holes around the leading edge of the blade were generally larger than the ducts in the aft section of the tip with the exception of the last trailing edge hole, which was comparable in size to the leading edge holes. Figure 3.11 depicts the area of each hole relative to the entire coolant cross-sectional flow area. This figure clearly illustrates the relative size of each duct as well as the dirt purge holes. The remainder of the tip geometry will be discussed in Chapter 4 with information pertaining

to the size of the flow domain, the boundary conditions used and other information involving the computational methodology. Computational results are discussed in Chapter 5 with benchmarking to experimental data in Chapter 7.

### **3.3 Turbine Blade Platform Simulations: Test Matrix and Geometry**

The turbine platform, like the tip, is also exposed to harsh conditions inside the gas turbine. Located just downstream of the combustor, extremely hot gases constantly bombard this region with temperatures that exceed the melting point of the blade metal. This requires the use active cooling to maintain metal temperatures at a safe level below that of their melting point. This cooling can be accomplished through the use of coolant both internally and externally.

Platform cooling can generally be accomplished through the use of a combination of film cooling holes and leakage flows from such things as the gutter and upstream and downstream rims. Figure 3.12 depicts the cross-section of a first stage turbine blade along with leakage flows from the gutter and rims. The gutter gap is a result of the manufacturing process in which single turbine blades are produced. When these blades are assembled in an engine there is a small gap between each platform through which air can travel. Some of this region can be blocked to prevent high pressure coolant air from reaching the passage, but there is generally a very thin gap (measuring less than 1mm at the 11x platform scaling) that is impossible to close. This leads to coolant entering the flow passage from the gutter (also known as the featherseal). Another region from which substantial leakage originates is around the rims of the platform. Located both upstream and downstream of the platform, these gaps result from the clearance distance that designers must add to allow for turbine rotation.

Film cooling holes around the platform involve small holes throughout much of the platform that exhaust cool air onto the endwall. These holes are generally angled such that the coolant does not exhaust directly into the main passage flow and mix out, but instead adheres to the wall creating a thin layer of cool air. This cool layer inhibits the interaction of hot mainstream gases with blade material ultimately providing

increased part life. Microcircuit ducts with film cooling, part of the focus of this research, is similar to the standard film cooling holes with several variations. These variations involve the coolant air first traveling through ducts located below the platform to provide internal cooling over sections of the endwall before finally exhausting into the passage flow and acting as film-cooling. Like the tip microcircuits, the platform microcircuits are a new technology that may appear in future blade designs, but at this point little is known about their effectiveness in cooling or their robustness. The internal cooling that results from the microcircuit is a function of both internal convection and conduction through the blade material. The internal coolant passages of the microcircuit are placed near the endwall surface, creating a thin metal layer between the cool air and hot mainstream gas to reduce the thermal resistance. The leakage flows coupled with coolant introduced through microcircuits will be presented as the second part of this study to evaluate cooling and flow patterns within the platform section of a turbine blade.

Figure 3.13 shows a diagram of the platform geometry looking down onto the platform. Flow is seen entering along the left side of the figure at a specified angle with each of the respective leakage points documented. Front rim and gutter leakage are the first coolant addition points with the front rim leakage entering via a backward facing step (discussed in more detail further into this section). Featherseal leakage is introduced between two platforms via a thin gap (measuring  $< 1\text{mm}$  at 11x scale) while microcircuit and aft rim and gutter leakage are also shown with a more in depth discussion to follow. Coolant to these entities was controlled by varying the flow to the four plenums located below the endwall. Each geometric entity has been assigned a number to allow for quick reference and will be used throughout this thesis.

Table 3.4 shows some important geometric features from the platform study. Included in this table are measurements of the pitch, chord, axial chord, inlet flow angle, blade rotation angle, inlet Reynolds number, the temperature difference between the mainstream and coolant flows and other various numbers of interest. As discussed for the tip in Section 3.2 these values were used in conjunction with the blade profile to construct computational models. Both the meshing and computational methodologies will be discussed in detail throughout Chapter 4 as general geometry and testing information is presented within this chapter.

Leakage flows from three different Pratt and Whitney engines will be investigated and are documented in Table 3.5. These engines include a PW4000, PW6000 and a new engine design the ActiveMC. The table shows flow values from four different areas that represent the four different plenums that were used for both experimental and computational work. The plenums were divided into the following entities: front leakage, aft leakage, featherseal leakage and microcircuit cooling. A complete platform test matrix is shown in Table 3.6 with additional information pertaining to geometry and testing information to be discussed within the section. It should be noted that the computations presented within this thesis have flowrates that are 1.9 times greater than engine flows as compared to 1.8 times engine flows as was originally desired. Detailed computational studies with five different geometries were performed to examine both flow and cooling characteristics at various blowing conditions.

Of the five geometries presented there were two different cooling methods under consideration: leakage cooling and microcircuit cooling. While Table 3.6 lists all of the geometries for which computations were simulated, Figure 3.14a-e shows the geometry associated with each of the cases. The first two cases listed in Table 3.6 are baseline cases consisting of no coolant flow. Termed “baseline–no fillet”, and “baseline-fillet” the only difference between these two models is the lack of a fillet on the first model. Previous work by Hermanson [2000] had shown that small manufacturing fillets have little, if any effect on the flow and cooling, but the fillet in this study is nearly three times larger than what was simulated by Hermanson. For this reason the fillets effect on the overall flow patterns and vortices throughout the main passage was examined. These cases have a flat endwall with no step.

The final three models of Table 3.6 and Figure 3.14 consisted of cases with microcircuit cooling with varying degrees of leakage flow, microcircuit only cooling without leakage, and cases with only leakage flow. The two cases with microcircuit cooling were run with all of the leakage flows or no leakage. This was done in order to isolate the microcircuit and understand its cooling ability while also looking at the entire cooling envelope, represented by leakage and microcircuit flows. The case with only microcircuit cooling did not utilize an upstream step configuration, and was run with a flat endwall. The final geometry, involving just leakage flows were run without

microcircuit cooling. For all cases in which there was leakage flow the front step configuration was utilized.

Figure 3.15 shows an isometric view of the platform. Depicted in this diagram is the backward facing step with front rim and gutter leakage, aft rim and gutter leakage and featherseal leakage in addition to the blade fillet and microcircuit ducts. The platform microcircuits consisted of two separate parts located along the pressure and suction sides of the blade with the exhaust slots visible in Figure 3.15 and shown in greater detail in Figure 3.16a-d. In Figure 3.16a-b the microcircuits are shown from the top (looking down on blade platform) while in Figure 3.16c-d the view is oriented to obtain an isometric view. The smaller of the two microcircuits exhausts coolant near the trailing edge of the pressure side while the second and larger microcircuit releases coolant near the trailing edge of the suction side. Their location was determined base on initial data showing the location of hot spots along the platform.

The size of the respective leakage gaps typically varies throughout the engine and is a strong function of engine temperature. All leakage gaps in this study were calculated assuming the engine was running at hot conditions making the leakage gaps smaller than what would be expected at cooler operation. Figure 3.1 illustrates a turbine blade as it would be made to sit in an engine. Within this figure, notice the platform and the region just below the platform that holds the blade during rotation. This figure serves to reinforce those concepts discussed in the previous paragraphs showing the reader the locations of leakage flow. On both the leading and trailing edge of the blade platform there is an overhang through which coolant flow travels without any obstructions as well as between two respective platforms.

Figure 3.17 diagrams the backward facing step as seen in the experimental and computational studies and is meant to match those conditions seen around the front rim of an actual platform configuration. Looking first at the side view, one can see the plenum feeding the rim with flow leaving the rim and interacting with the mainstream passage flow. This geometry was pulled directly from a turbine blade and should very well represent those conditions seen in an engine. All dimensions are made relative to the thickness of the slot which in experiments measures 24mm. The top view shows much of the same as was seen with the side view with the front gutter and featherseal locations

also becoming visible. The front gutter leakage is present only at the interface between two platforms meaning the gutter appears at one pitch length intervals while the rim leakage is continuous across the pitch.

The aft leakage configuration is seen in Figure 3.18. While engine geometry for the aft rim configuration would ideally be similar to that of the front configuration having a step-like design, it was determined that the overall effects were not as critical to the overall scope of the research. Much of the cooling from the aft rim is generally swept away with no platform effects so the some approximations in the geometry can be made. The only cooling benefit that may come from the aft leakage potentially occurs from the aft gutter which in fact shares a plenum with the aft rim thereby requiring the aft rim to be tested as well. A top view of the aft rim and gutter leakage shows coolant leaving both the featherseal and aft plenums and interacting with hot mainstream gasses. Dimensions are noted and are once again referenced to the thickness of the aft slot, measuring 24mm across.

Locations of some important geometric entities are noted in Figure 3.19. The plot has been non-dimensionalized in the x-direction by the axial chord and by the pitch in the y-direction. Specific locations of the microcircuit slots, gutter and rims are noted as well as the front step. The blade stagnation point is located at  $x/B_x = 0$  with the trailing edge located at  $x/B_x = 1.0$ . All  $x/B_x < 0$  are located upstream of the blade while those values of  $x/B_x > 0$  are downstream.

Figure 3.20 shows the relative size of each coolant exhaust exit as a percentage of the total coolant flow area. The front and aft rim leakage account for approximately 90% of the area from which coolant can pass while the remainder of the coolant is left to travel through 10% of the overall area. This creates some interesting phenomena in terms of the coolant velocities. The large area of the rim leakage (front and aft) while generally greater than those of other cooling sources leaves through a large area thus creating lower velocities than what was seen for the other entities. Investigation of flow mixing due to variations in momentum should be very interesting to look at in the following chapters. Table 3.7 defines the average mass flux, momentum flux and velocity ratios for each of the nine cases that were investigated with coolant flow. The calculation of these values were discussed in Section 3.2 and also shown in equations 3.2 – 3.4.

An overview of the platform test matrix has been outlined within this section. Remaining information concerning platform meshing and solution methodologies will be presented in Chapter 4 with detailed results shown and discussed in Chapter 6.

**Table 3.1.** Geometry and flow conditions for the tip.

| Parameter                        | Value   |
|----------------------------------|---------|
| Scaling Factor                   | 12X     |
| Axial chord, $B_x$               | 0.35m   |
| True Chord, C                    | 0.53m   |
| Pitch, P                         | 0.43m   |
| Span, S                          | 0.55m   |
| Re                               | 2.1E+05 |
| Inlet Angle, $\theta$            | 16.5°   |
| Blade Angle, $\phi$              | 50°     |
| Coolant to Mainstream $\Delta T$ | 25°     |
| Small tip gap, h                 | 0.003m  |
| Large tip gap, H                 | 0.009m  |

**Table 3.2.** Geometry, tip gap size and coolant flow for each tip gap geometry considered.

| Geometry                                             | Tip Gap<br>(% Span) | Coolant Flow<br>(% Passage Flow) |
|------------------------------------------------------|---------------------|----------------------------------|
| <b>Flat Tip</b>                                      | Small<br>0.54%      | 0                                |
|                                                      | Large<br>1.63%      | 0                                |
| <b>Dirt Purge<br/>Cavity</b>                         | Small<br>0.54%      | 0                                |
|                                                      | Large<br>1.63%      | 0                                |
| <b>Dirt Purge<br/>Cavity Blowing</b>                 | Small<br>0.54%      | 0.05, 0.10, 0.19, 0.29, 0.38     |
|                                                      | Large<br>1.63%      | 0.05, 0.10, 0.19, 0.29, 0.38     |
| <b>Microcircuit &amp;<br/>Dirt Purge<br/>Blowing</b> | Small<br>0.54%      | 0.5, 1.0, 1.5, 2.0               |
|                                                      | Large<br>1.63%      | 0.5, 1.0, 1.5, 2.0               |

**Table 3.3.** Average mass flux, momentum flux and velocity ratios for all blowing cases along the tip.

| Geometry                          | Total Coolant Flow (%) | Average         |                     |                |
|-----------------------------------|------------------------|-----------------|---------------------|----------------|
|                                   |                        | Mass Flux Ratio | Momentum Flux Ratio | Velocity Ratio |
| Dirt Purge Blowing                | 0.05                   | 0.80            | 0.58                | 0.72           |
|                                   | 0.10                   | 1.60            | 2.31                | 1.44           |
|                                   | 0.19                   | 3.04            | 8.34                | 2.74           |
|                                   | 0.29                   | 4.65            | 19.43               | 4.18           |
|                                   | 0.38                   | 6.09            | 33.36               | 5.48           |
| Microcircuit & Dirt Purge Blowing | 0.5                    | 0.91            | 0.74                | 0.82           |
|                                   | 1.0                    | 1.82            | 2.98                | 1.64           |
|                                   | 1.5                    | 2.73            | 6.70                | 2.45           |
|                                   | 2.0                    | 3.64            | 11.91               | 3.27           |

**Table 3.4.** Geometry and flow conditions for the platform.

| Parameter                        | Value   |
|----------------------------------|---------|
| Scaling Factor                   | 11X     |
| Axial chord, $B_x$               | 0.43m   |
| True Chord, C                    | 0.45m   |
| Pitch, P                         | 0.34m   |
| Span, S                          | 0.55m   |
| Re                               | 3.0E+05 |
| Inlet Angle, $\theta$            | 19.2°   |
| Blade Angle, $\phi$              | 20°     |
| Coolant to Mainstream $\Delta T$ | 25 K    |
| Featherseal thickness            | 0.001m  |
| Rim leakage thickness            | 0.024m  |
| Gutter thickness                 | 0.003m  |

**Table 3.5.** Coolant flowrates used for platform testing.

| Geometry      | Flowrates |        |        |
|---------------|-----------|--------|--------|
|               | ActiveMC  | PW6000 | PW4000 |
| Microcircuit  | 0.48%     | 0.48%  | 0.48%  |
| Front Leakage | 1.67%     | 2.05%  | 2.63%  |
| Featherseal   | 0.37%     | 0.77%  | 0.53%  |
| Aft Leakage   | 1.84%     | 1.46%  | 1.47%  |
| Total         | 4.36%     | 4.76%  | 5.11%  |

**Table 3.6.** Geometry, front rim configuration, and coolant flows for platform tests.

| Geometry               | Front Rim Configuration | Computational or Experimental | Coolant Flow                                                      |
|------------------------|-------------------------|-------------------------------|-------------------------------------------------------------------|
| Baseline (no fillet)   | No Step                 | Computational                 | 0                                                                 |
| Baseline (fillet)      | No Step                 | Computational                 | 0                                                                 |
| Leakage                | Step                    | Both                          | ActiveMC - 1.5% aft<br>ActiveMC - 2.0% aft<br>ActiveMC - 2.5% aft |
| Microcircuit           | No Step                 | Computational                 | ActiveMC                                                          |
| Microcircuit & Leakage | Step                    | Both                          | ActiveMC<br>PW6000<br>PW4000                                      |

**Table 3.7.** Average mass flux, momentum flux and velocity ratios for all blowing cases along the platform.

| Geometry               | Coolant Flow    | Total Coolant Flow (%) | Average         |                     |                |
|------------------------|-----------------|------------------------|-----------------|---------------------|----------------|
|                        |                 |                        | Mass Flux Ratio | Momentum Flux Ratio | Velocity Ratio |
| Leakage                | ActiveMC - 1.5% | 3.54                   | 0.45            | 0.19                | 0.41           |
|                        | ActiveMC - 2.0% | 4.04                   | 0.52            | 0.24                | 0.47           |
|                        | ActiveMC - 2.5% | 4.54                   | 0.58            | 0.31                | 0.52           |
| Microcircuit & Leakage | ActiveMC        | 4.36                   | 0.53            | 0.25                | 0.48           |
|                        | PW6000          | 4.76                   | 0.58            | 0.30                | 0.52           |
|                        | PW4000          | 5.11                   | 0.62            | 0.35                | 0.56           |
| Microcircuit           | ActiveMC        | 0.48                   | 1.11            | 1.11                | 1.00           |

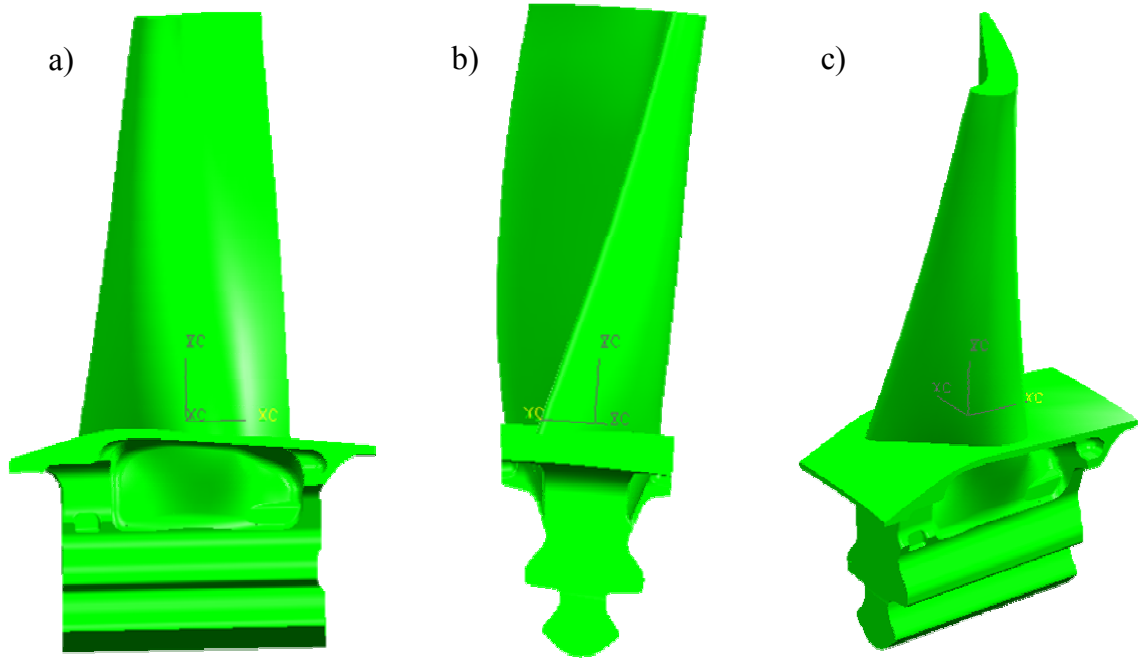


**Figure 3.1a-c.** Turbine blade shown from three different views including a) side, b) front, and c) isometric.

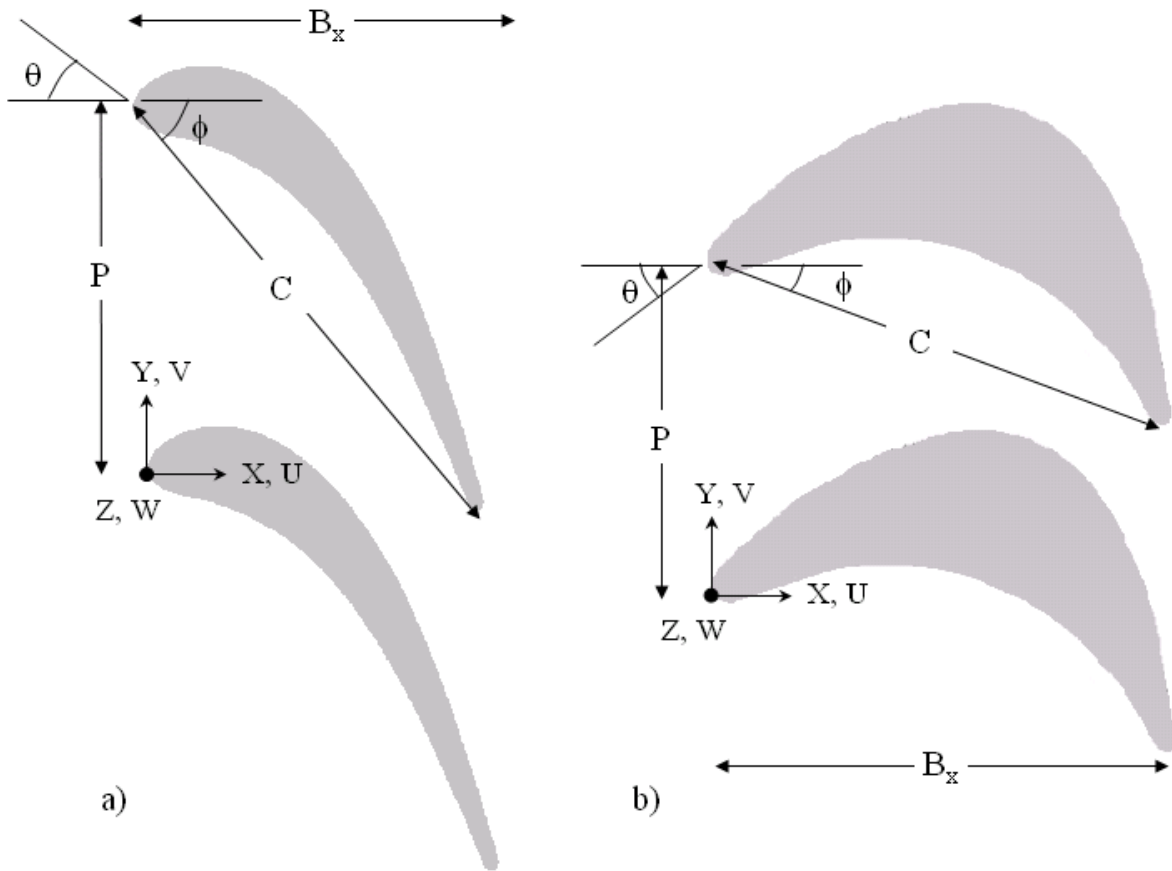


**Figure 3.2a-b.** Important geometric features within a turbine blade including pitch, axial chord, true chord, flow entrance angle, and blade angle for a) tip geometry, and b) platform geometry.

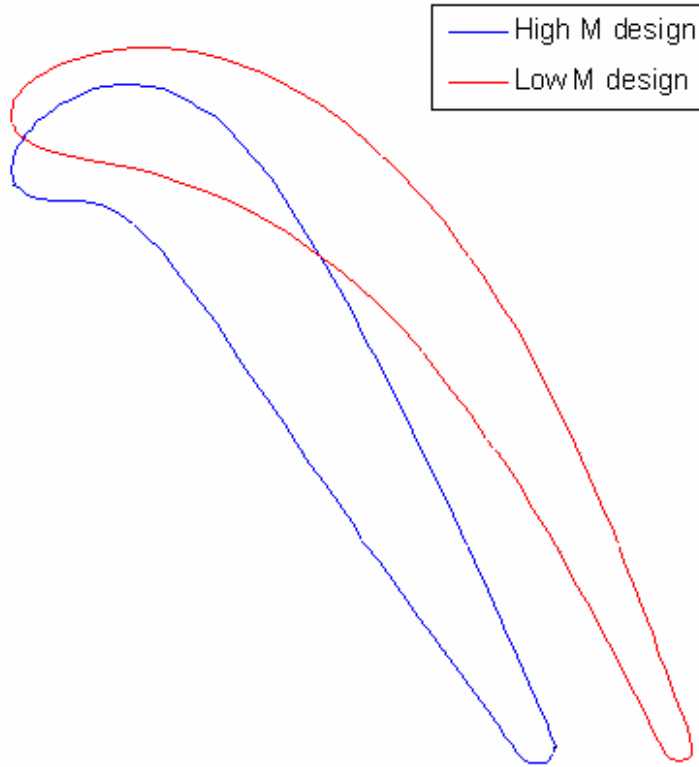


**Figure 3.3.** Two different designs for a turbine blade tip cross-section with the high-speed (engine) blade shown in blue and the low-speed (experimental) blade shown in red (Praisner, 2002).

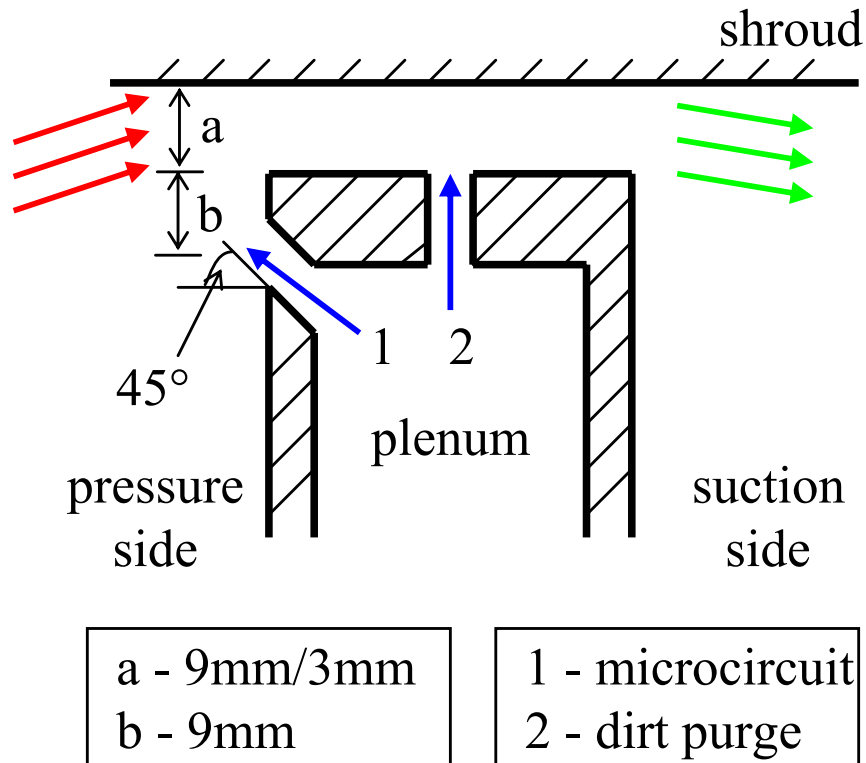


**Figure 3.4.** Cross-section of the tip region of a turbine blade showing the tip leakage in relation to the microcircuit and dirt purge cooling.

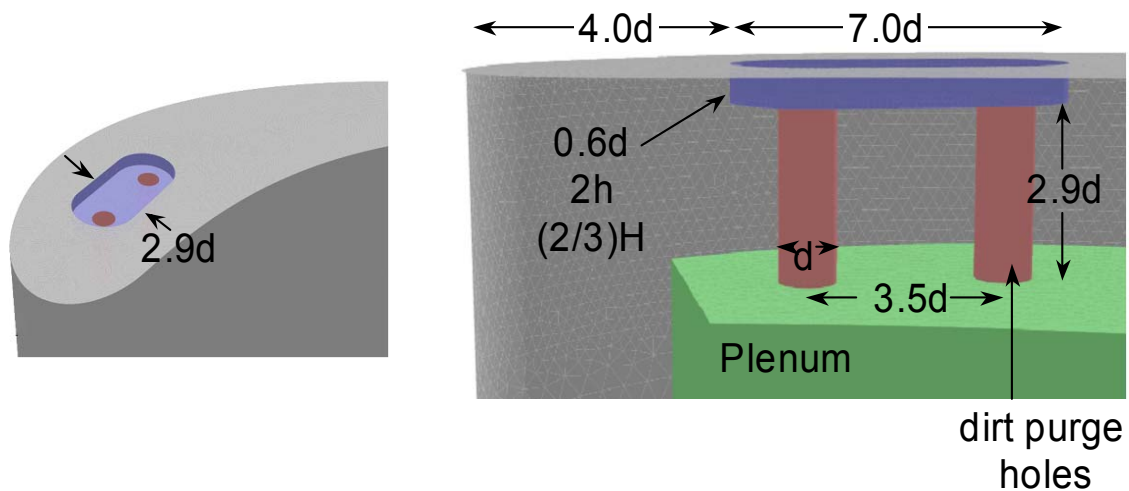


**Figure 3.5.** Dirt purge geometry showing an isometric top view on the left and a side view with the pressure side sheathing removed.

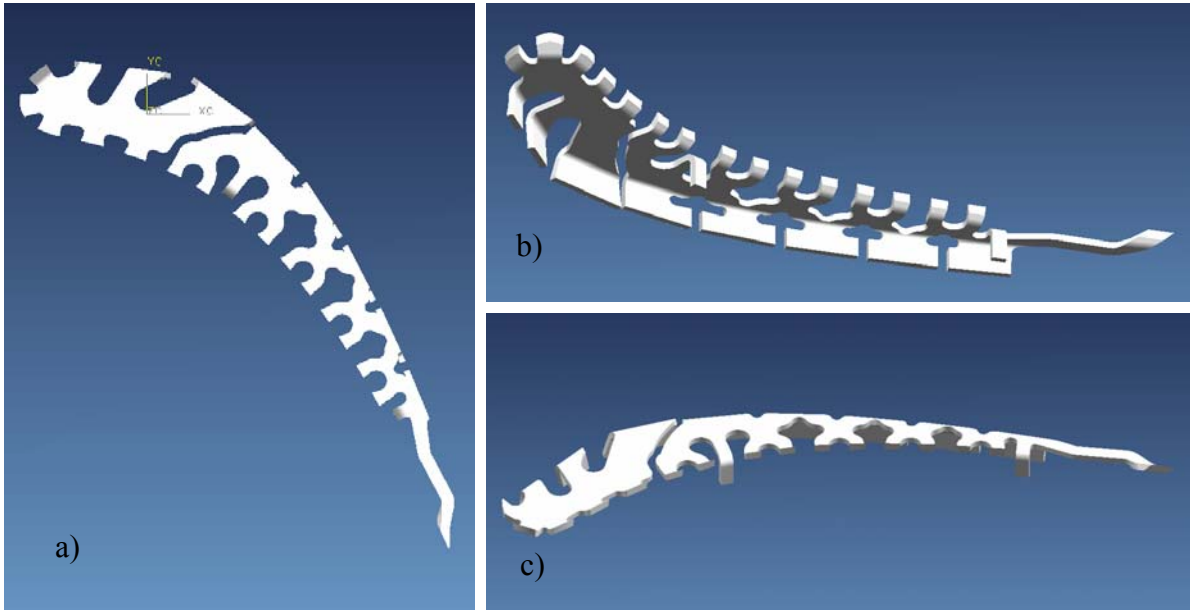


**Figure 3.6a-c.** Images of the tip microcircuit geometry from a a) top view and b-c) two isometric views looking at the side from above and below the microcircuit.

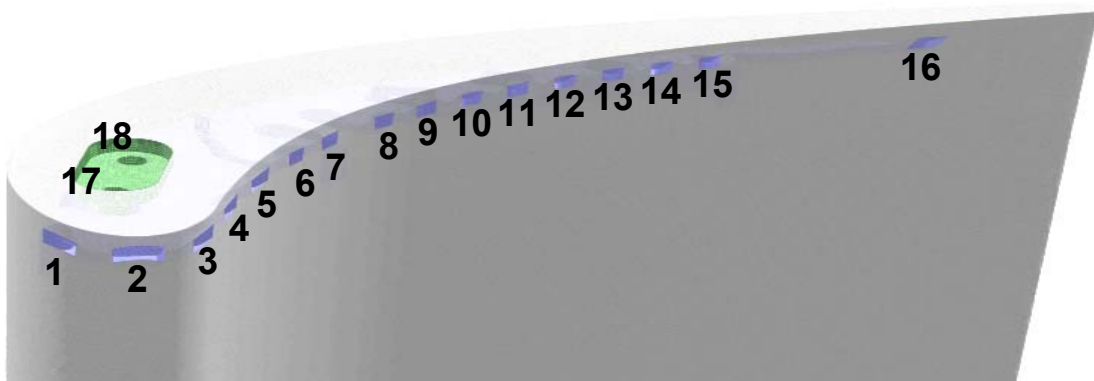


**Figure 3.7.** Tip microcircuit numbering scheme for referencing various flow ducts with microcircuit exits numbered 1-16 and the dirt purge holes 17 and 18.

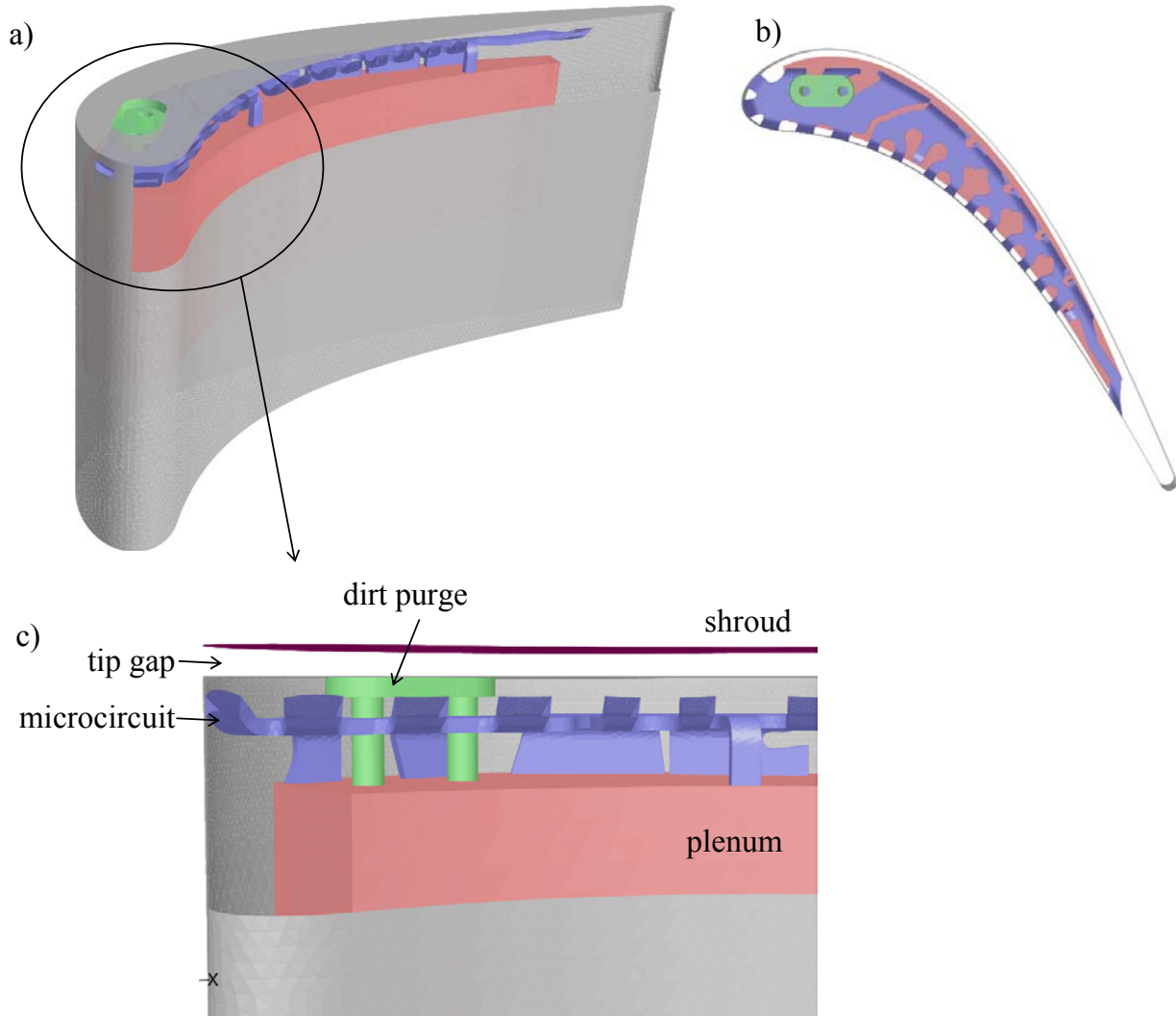


**Figure 3.8a-c.** Microcircuit and dirt purge shown within a blade looking from a) an isometric view, b) top view and c) side view. Part of the side sheathing removed has been removed to allow internal views.

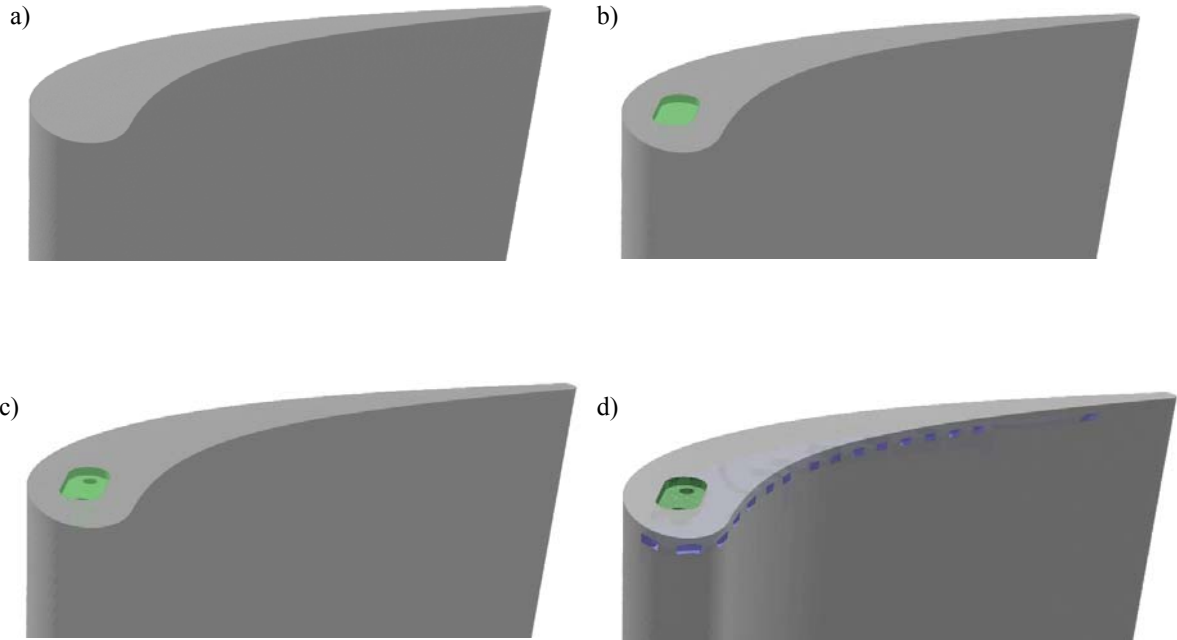


**Figure 3.9a-c.** Four different blade geometries that were studied for tip computations which include a) flat tip, b) dirt purge cavity within tip, c) dirt purge cavity with blowing, and d) microcircuit and dirt purge with blowing.

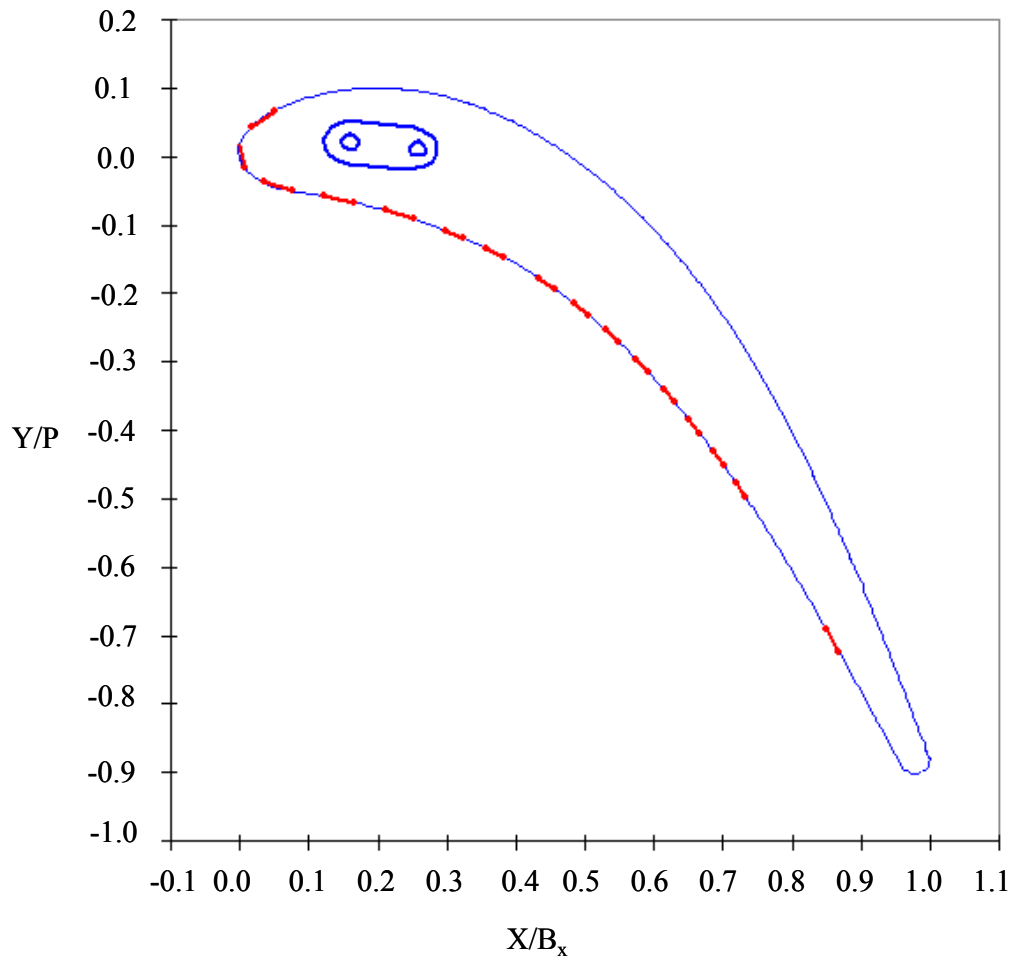


**Figure 3.10.** Non-dimensional cross section of the tip geometry showing microcircuit and dirt purge locations where the horizontal and vertical planes have divided by the axial chord and pitch, respectively.

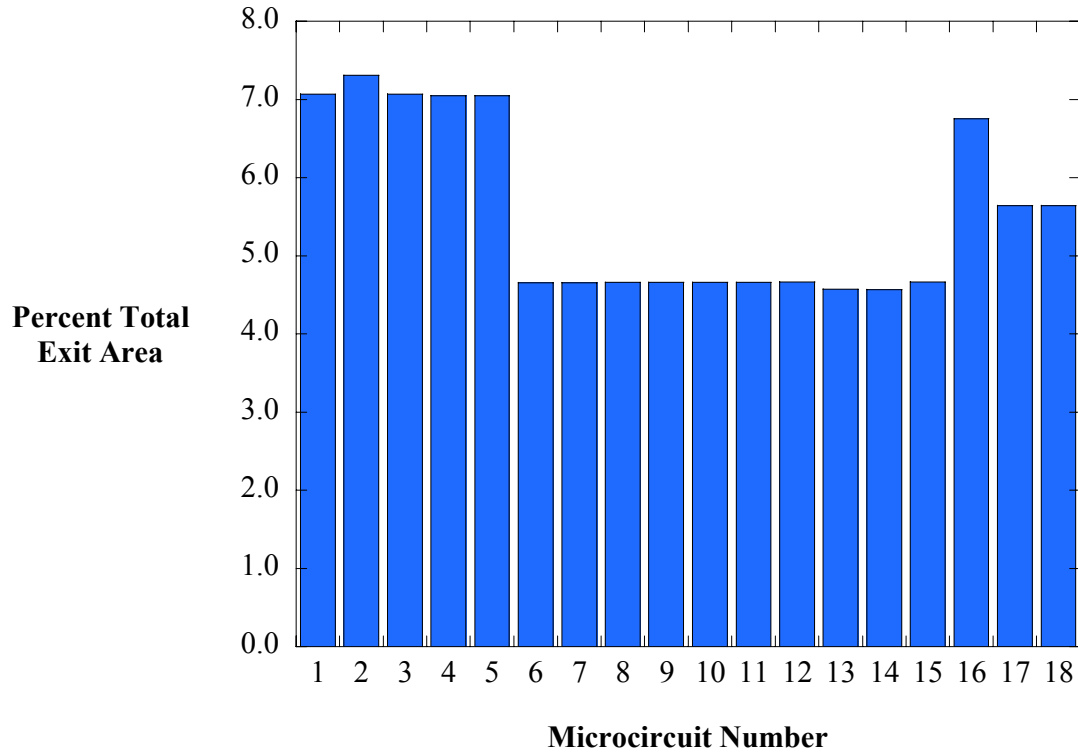


**Figure 3.11.** Exit area of each tip microcircuit and dirt purge hole when compared to the entire coolant flow area.

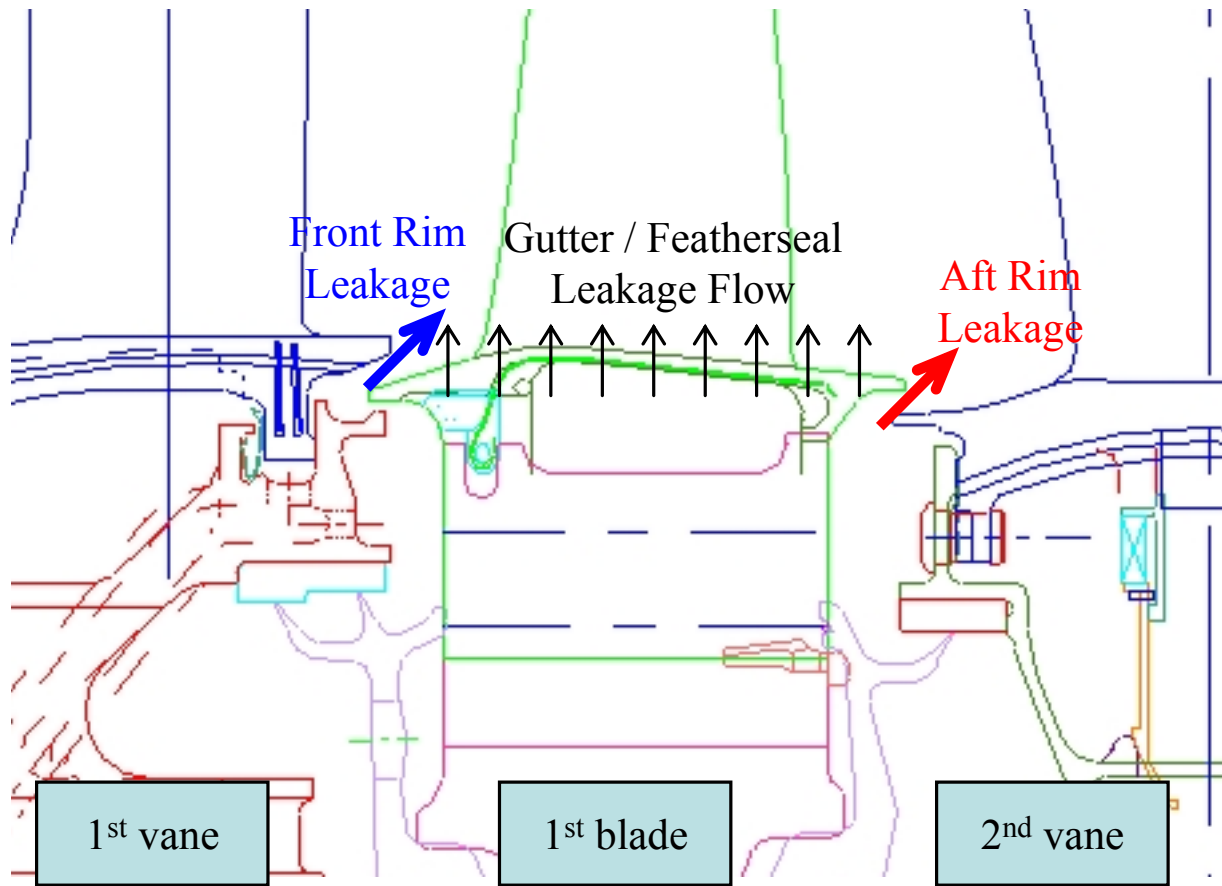


**Figure3.12.** Schematic diagram of a first stage turbine rotor blade with upstream and downstream stator vanes. Gutter and rim leakage flows are shown in their relative positions.

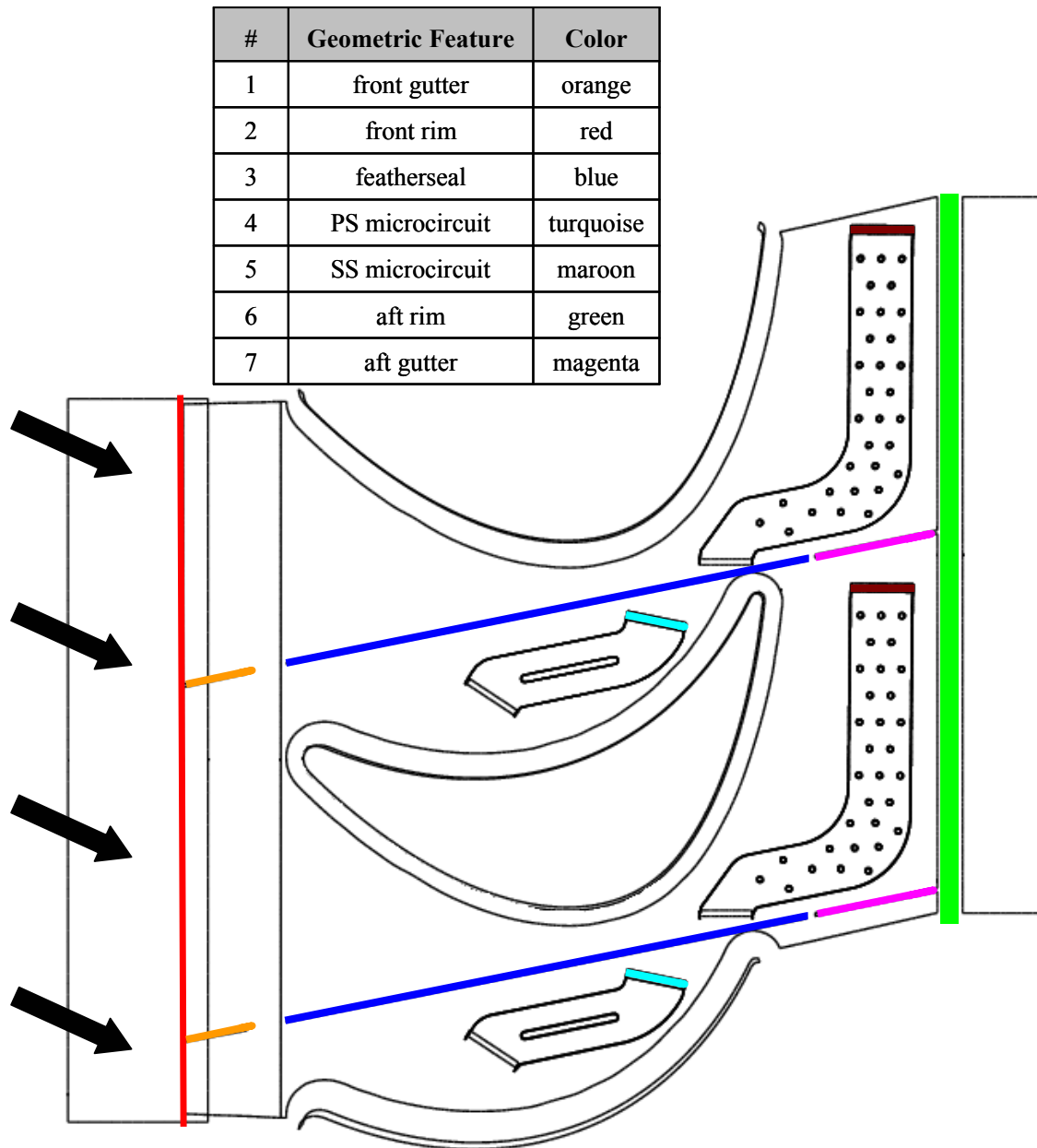


**Figure 3.13.** Various leakage flows throughout the platform geometry. Each has been assigned a reference number and a unique color.

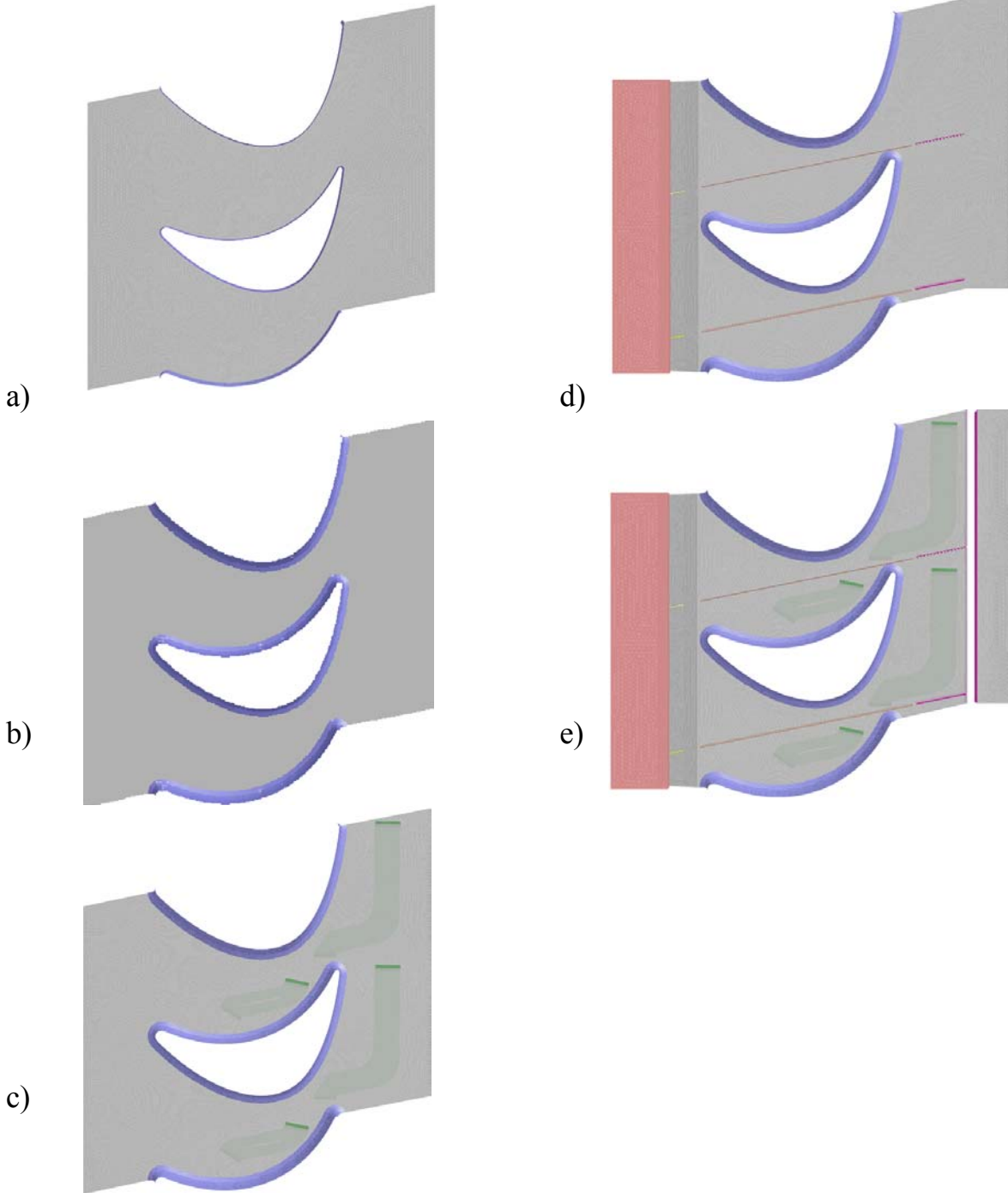


**Figure 3.14a-e.** Five different blade geometries were studied for hub computations including a) baseline – no fillet, b) baseline – fillet, c) microcircuit only, d) front, aft and featherseal leakage, and e) front, aft and featherseal leakage combined with microcircuit flow cooling.

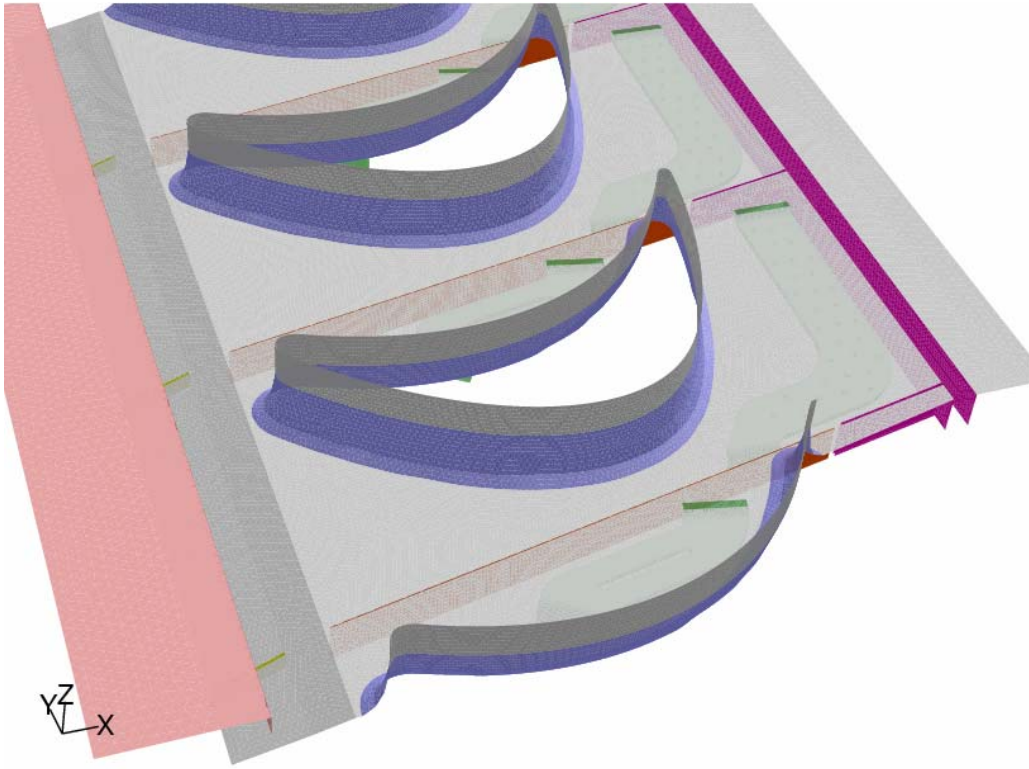


**Figure 3.15.** Isometric view of the platform geometry showing featherseal leakage (orange), front rim leakage (pink and yellow), aft rim leakage (violet) and microcircuit ducts (green) with the blade fillet (blue).

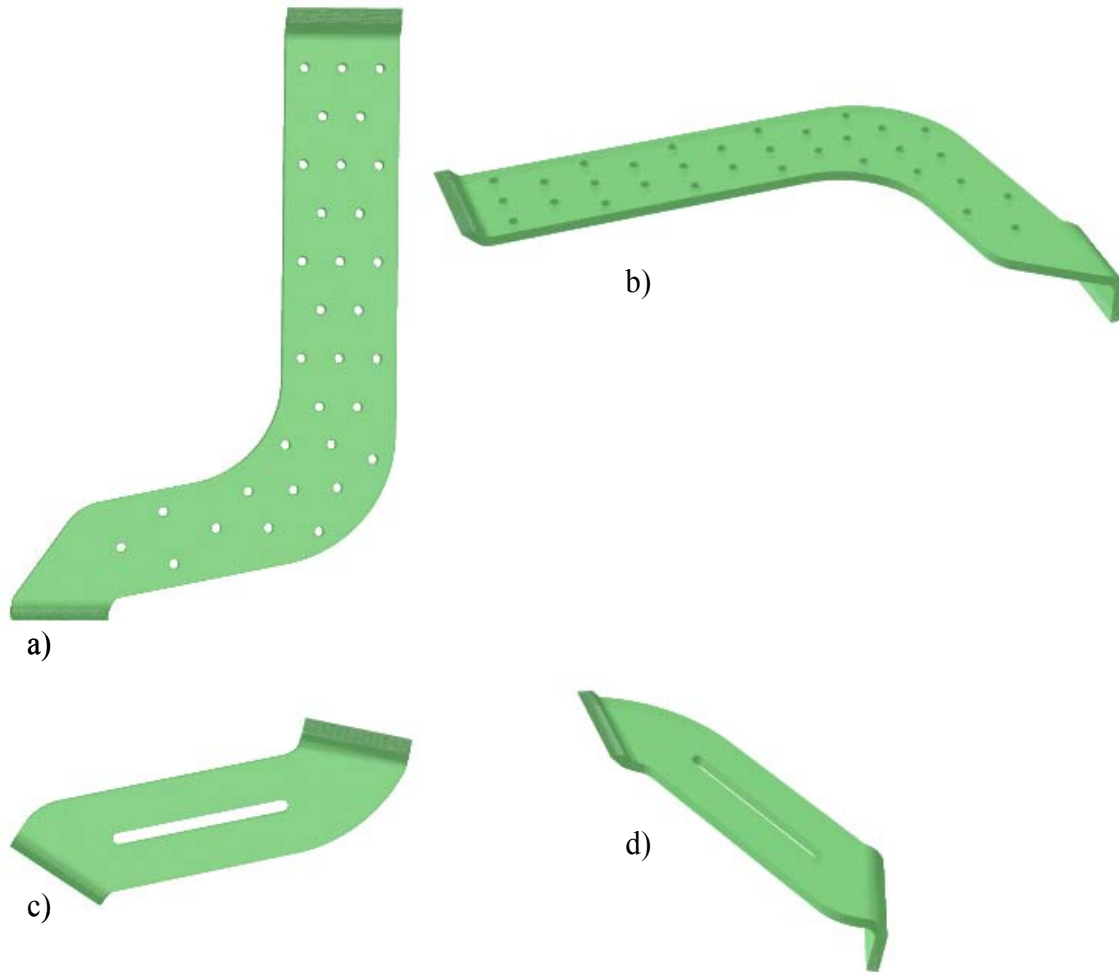
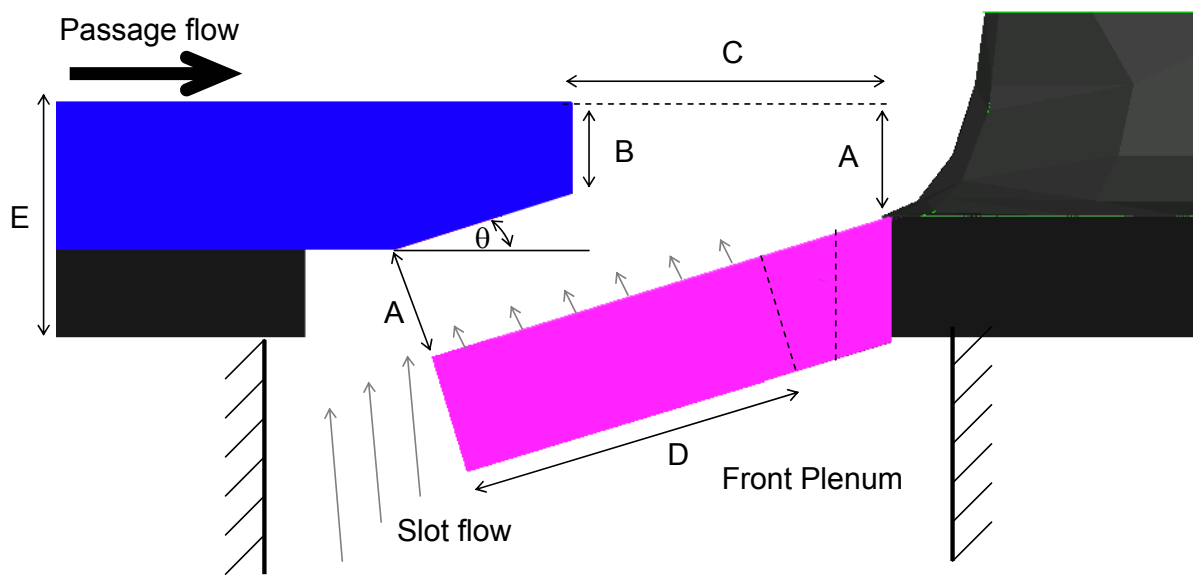


**Figure 3.16a-d.** Images of the two platform microcircuits looking at a) top view of suction side circuit, b) isometric view of suction side circuit, c) top view of pressure side circuit, and d) isometric view of pressure side circuit.

| Geometry | Length |
|----------|--------|
| A        | t      |
| B        | 0.79t  |
| C        | 2.67t  |
| D        | 2.67t  |
| E        | 1.58t  |
| $\theta$ | 17°    |

Side View



Top View

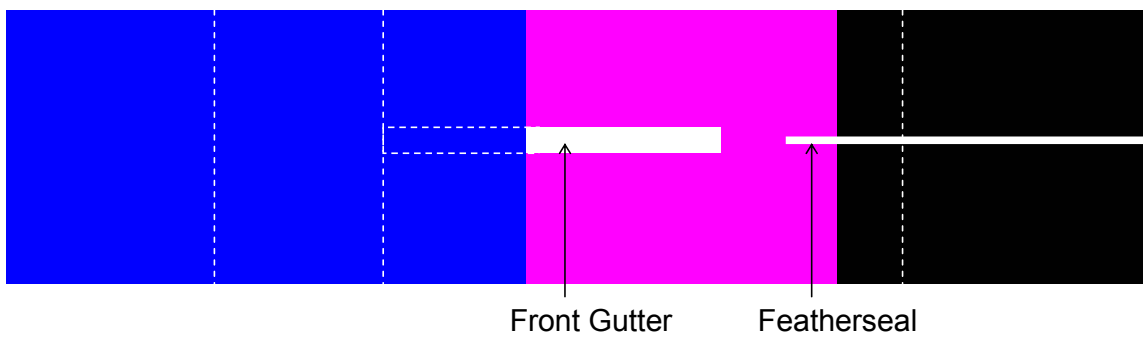
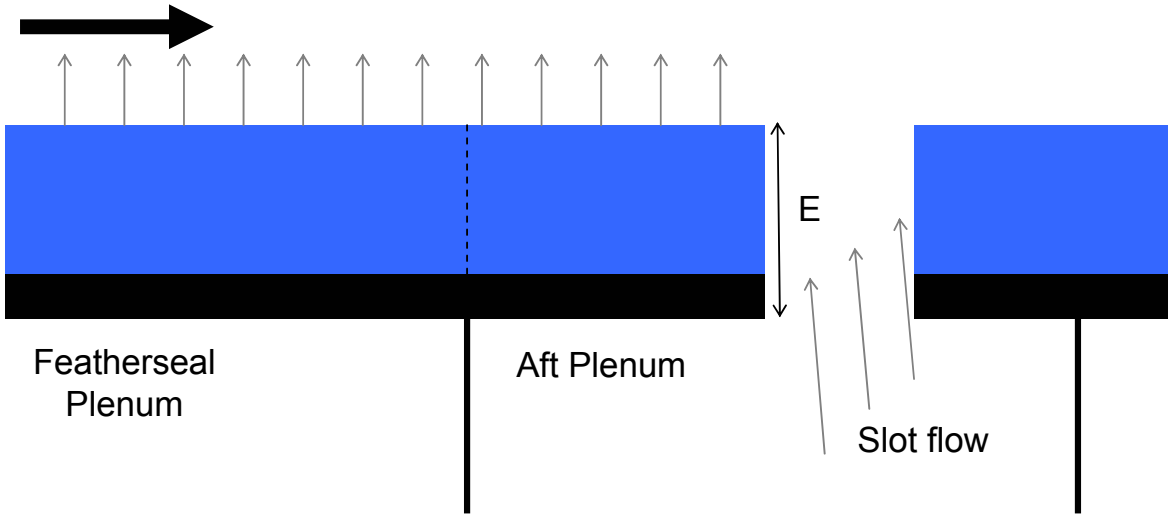


**Figure 3.17.** Side and top view of the platform front rim design with a backward facing step.

| Geometry | Length  |
|----------|---------|
| A        | $t$     |
| B        | $3.75t$ |
| C        | $t$     |
| D        | $0.04t$ |
| E        | $1.58t$ |

Side View

Passage flow



Top View

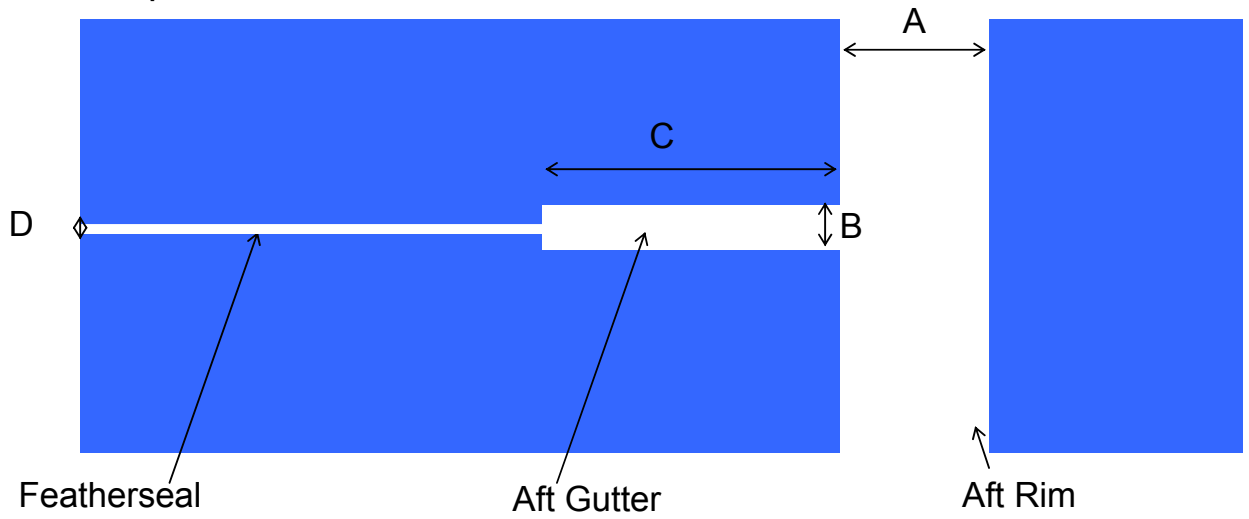
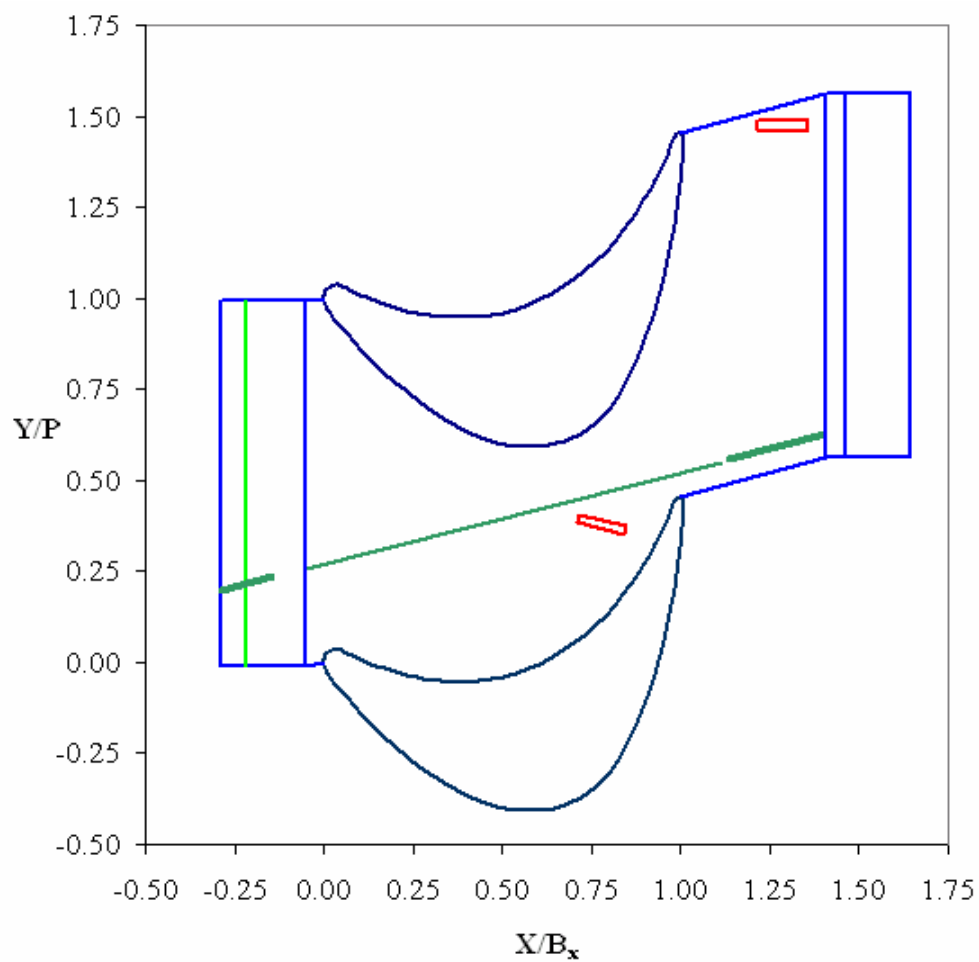
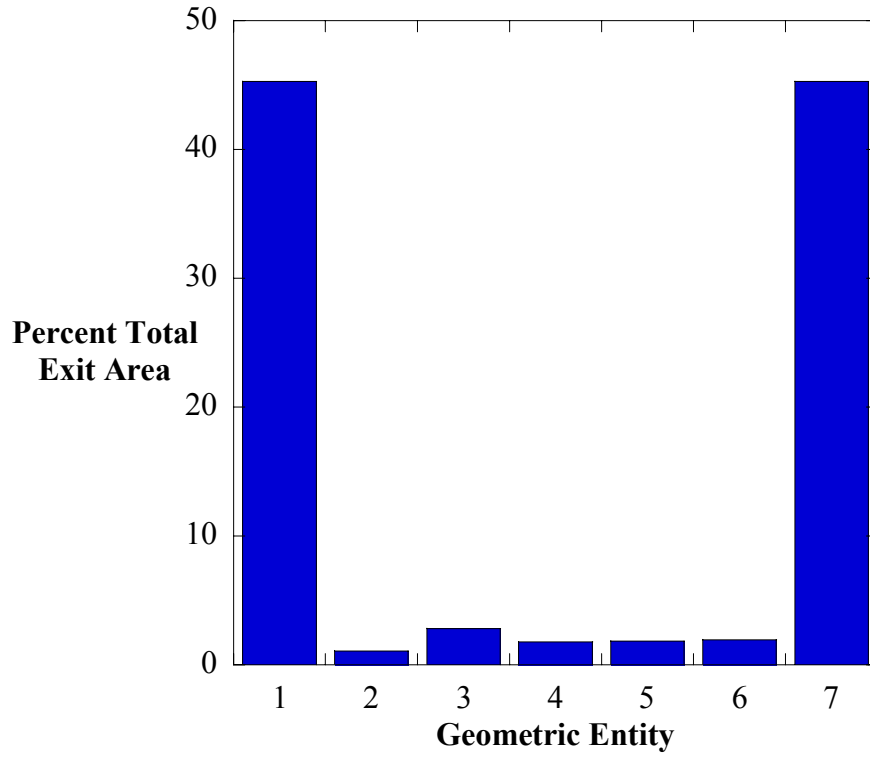


Figure 3.18. Side and top view of the platform aft rim design.



**Figure 3.19.** Gutter geometry and microcircuit locations shown on a non-dimensional plot with microcircuit exhausts shown in red, gutter leakage as dark green and the step overhang location shown as light green.



**Figure 3.20.** Exit area of each hub microcircuit and leakage gap when compared to the entire coolant flow area. These numbers correspond to the geometry of Figure 3.13

## Chapter 4

### Computational Methodology

Computational Fluid Dynamics, commonly known as CFD has become an important tool used for the design and analysis of thermal-fluid systems over the last several decades saving significant time and money for the companies who choose to take advantage of this capability. Increases in computing power have permitted more detailed calculations to be undertaken in significantly less time leading to an expanded envelope for computational modeling.

In many cases, fluid flow and heat transfer phenomena in a realistic environment are very difficult to predict and experimentally study. The advantage of a computational analysis is the relative quickness and low cost when compared to experimental work. In the time it takes to develop, build, troubleshoot and analyze data from an experiment, an entire test matrix can be examined computationally. This is not to say that the computational results are entirely accurate because in some cases they only provide a limited view of the entire picture. CFD can be extremely valuable for the prediction of general trends and/or flow phenomena that many times cannot be examined during experimental testing.

Ultimately, it is desirable to continue the development of newer and more accurate CFD algorithms while benchmarking current computational packages. This accuracy cannot be developed without extensive benchmarking and comparison of experimental and computational results as well as the continued investment in more powerful modeling programs. A detailed summary of the CFD methodology and techniques employed during this study will be discussed in the following chapter.

#### 4.1 CFD Overview and Methodology

CFD has become an integral part of the research and design process as more work is undertaken to benchmark and study various flows. The study of fluid dynamics and

heat transfer while extremely complicated can be summarized by a handful of equations. Unfortunately, the mathematical complexity of many of these equations does not permit us to analytically solve for exact solutions. Only through simplification and/or approximations can we begin to solve many fluid dynamics and heat transfer problems.

The computational process can be divided into three main components consisting of a pre-processing stage, solver stage, and finally a post-processing stage. The pre-processing involves constructing the computational domain. Included in this is the geometric assembly of the model, the meshing, and finally the application of boundary conditions. The solver stage involves sending the model to a CFD program and solving the governing equations to provide results. The results from the solver are then analyzed in a post-processing stage.

It is extremely desirable to perform a comparison of CFD and experimental work for benchmarking to determine the viability of the computer models. For this reason the computational models of this study were developed to coincide with identical experimental work in order to perform a one-to-one comparison of the respective results. The experimental work dictated most of the computational geometry and modeling conditions due to equipment limitations and test specifications from the project sponsor. After some initial dialogue concerning the desired outcome of experimental testing the computational domain and boundary conditions quickly fell into place and will be discussed in detail throughout this chapter.

Initial work focused on fitting an adequate number of turbine flow passages into the wind tunnel so that periodic conditions could be established. It was necessary to have at least two passages in the tunnel to achieve periodicity, with the flow to each passage controlled by tailboards and a flexible outer wall. It was decided to test two passages for the tip geometry (three blades) and three passages for the hub (four blades). This established the scaling factor (12X and 11X scale factor for the tip and platform, respectively) with significant consideration given to the ability to match a given Reynolds number. With the geometry set and inlet conditions known it is possible to establish a computational model.

An important part in any computational simulation is developing accurate boundary conditions for the models. Figures 4.1a-b depict the flow domains for the tip

and platform geometry that were established. All computations were performed on a single turbine blade exposed to periodic conditions along all boundaries in the pitch direction. Inlet conditions to the tip model were set as a uniform inlet velocity at approximately one chord upstream of the blade while the platform models were exposed to a specified velocity profile. Flow angles were set to match those conditions of the experiment. Turbulence levels and mixing length were set to 1% and 0.1 m for the tip and 10% and 0.1m for the platform models. An outflow boundary condition was set approximately 1.5 chord lengths downstream of the blade, so as not to interfere with the trailing edge region. In Figure 4.1a one should take note of the periodic conditions and location of the blade relative to the inlet and exit conditions. As will be discussed later in more detail, there is a frictionless wall located on the mid-span since only half of the span was modeled. In the platform model of Figure 4.1b many of the same boundary conditions are present with the only notable difference being at the mid-span, the frictionless wall of the tip model has been replaced by a symmetry condition, as all models were only run to mid-span. For all cases mass flow inlet conditions feed the plenums.

Initially, two-dimensional models were computed in order to compare pressure distributions around the turbine blade surface provided by Pratt and Whitney (P&W). This served as an initial check to ensure that boundary conditions and methodologies between P&W and Virginia Tech were consistent. Various meshes and flow conditions were considered using the same geometry to study grid independence and variations between turbulent and inviscid flow solutions. The results from two of these studies are presented in Figure 4.2a-b with non-dimensional pressure plotted against the distance along the blade. Figure 4.2a shows the tip study while Figure 4.2b shows the platform study. Within each of these plots are two meshes that equate to 11,600 and 45,800 cells for the tip cases and 10,200 and 40,100 cells for platform cases. Each mesh was run with two different flow conditions, inviscid and turbulent. In both figures the stagnation point is located at  $s/s_{\max} = 0$ , the point of highest pressure while the pressure side of the blade is located on the negative side of the horizontal axis and the suction side on the positive horizontal axis. The only significant variation between the simulations of Figure 4.2a occurs along the suction side of the blade from  $s/s_{\max} = 0.5$  to  $s/s_{\max} = 1.0$  with relatively

good agreement everywhere else. Figure 4.2b shows four platform predictions plotted against the Pratt and Whitney [Praisner, 2002] pressure distribution. The only significant variation occurs on the suction side of the blade when  $s/s_{\max} = 0.6$  to  $s/s_{\max} = 1.0$ . Pressure variability along the latter half of the suction side is fairly common between all of the models and points out an area that is difficult to predict.

After matching the pressure distribution around the blade, work quickly progressed to three-dimensional testing of the entire turbine passage. As discussed in Chapter 3, this project involved investigating multiple geometries both computationally, which is the emphasis of this thesis and experimentally which was undertaken by Couch [2003], Christophel [2003] and Ranson [2004]. Simulations of the entire blade span from both platform and tip models indicated that it was not necessary to run simulations of the entire span as the flow-field around the mid-span was not affected by the specific areas of interest located at either the tip (shroud) or platform (endwall). This enabled a significant savings in cells and allowed subsequent models to be run from the mid-span to the area of interest.

Figure 4.3 shows the pressure distribution around the blade tip geometry for three different computational cases. The first case is a two-dimensional model while the other two cases involve three-dimensional models run with a small and large tip gap, respectively. Both of the three-dimensional models were run with only half of the span being modeled with non-dimensional pressure around the mid-span plotted to explore any tip effects at the mid-span. Notice that there is little difference in the pressure distribution around the blades for each of the respective cases. With the pressure constant at the mid-span when looking at a two-dimensional or three-dimensional model it was not necessary to computationally model from the mid-span to the endwall for tip tests. This same phenomena was also seen for the platform, allowing models to be run from the mid-span to the endwall.

The computational domain for the tip is shown in Figure 4.4 and will be briefly highlighted with a more detailed discussion to follow within the thesis. The domain consisted of coolant flow entering a plenum within the blade cavity, which provided coolant flow to the tip region of the blade at a temperature difference of 25 K below that of the passage flow (matching that simulated in the experiments). The amount of coolant

flow entering the model was specified as a mass flowrate boundary condition. Flow entered the tip region by several paths, which varied based on the geometry being studied. These paths consisted of two dirt purge holes located in the leading edge of the blade and sixteen microcircuit holes that generally exhausted flow on the pressure side of the blade as discussed in Chapter 3.

The platform computational model is shown in Figure 4.5 and consisted of coolant flow entering one of four plenums located below the endwall via a mass flux inlet. As with the tip tests coolant could travel through several paths to reach the main passage, which varied based on the tests being run. These flow paths consisted of front leakage (rim and gutter), aft leakage (rim and gutter), featherseal leakage and microcircuit cooling ducts. Additional geometric information will be discussed throughout this chapter.

## **4.2 Governing Equations and Solution Methods**

A commercially available CFD code, Fluent 6.0 [2002] was used to perform all simulations. Fluent is a pressure-based, incompressible flow solver that can be used with structured or unstructured grids. An unstructured grid was used for the work presented within this study. Solutions were obtained by numerically solving the Reynolds-Averaged Navier-Stokes (RANS) and energy equations through a control volume technique. All geometric construction and meshing was performed with GAMBIT, a meshing package provided with the CFD software.

Fluent offers the ability to obtain solutions through a segregated solution algorithm (FLUENT/UNS) with a control volume based technique or with the use of a coupled solver (RAMPANT) also using a control volume technique. The basic premise behind the segregated solver, which was used exclusively in this study involves the integration of the mass, momentum, energy and turbulence equations for each unknown variable. The discretized equations are then linearized with a solution of the resulting system of linear equations providing updated results to the unknown variables.

The governing equations are solved sequentially employing an implicit form of linearization where, for each variable the value of interest in each cell is computed through the use of equations that use both known and unknown values from various neighboring cells. Ultimately, each unknown appears in a series of equations that must be solved simultaneously. A converged solution takes many iterations and includes the following general process:

- (1) fluid properties are updated with the current solution,
- (2) the u, v, w momentum equations are each solved with current values for pressure and mass fluxes to update the velocity field,
- (3) the velocities from step one may not locally satisfy the continuity equation so adjustments are made by correction equations so that continuity is satisfied,
- (4) scalar equations are solved for such things as turbulence and energy with the previously updated values from other variables, and
- (5) a convergence check is made of the equations.

Fluent offers several discretization techniques for the convective terms of each governing equation. Using the segregated solver, as was done for this study, the operator may choose to have either first or second order discretization of terms. The first order discretization is generally acceptable for simple flows when the grid is aligned with the flow and a quadrilateral or hexahedral grid is in place. A second order discretization method reduces errors over the first order methods, while generally increasing the difficulty to obtain a converged solution. For triangular and tetrahedral grids when the flow is not aligned with the grid, a second order method is recommended for superior results. In most cases performed within this study the second order discretization is preferred due to its increased accuracy and it was used for the simulations done in this study.

Pressure and velocity were coupled with the Semi-Implicit Method for Pressure Linked Equations (SIMPLE) algorithm. SIMPLE uses a relationship between velocity and pressure corrections to obtain mass conservation and a pressure field.

Before starting any computations Fluent requires the flow to be initialized based on some condition within the model. This initialization process acts as an initial guess to the solution flow field. For all computational simulations the flow field was initialized by the inlet conditions to the model.

Several times a solution could not be obtained due to the inability of the residual values to converge to an appropriate level. In cases where this issue was prevalent it was possible to adjust under-relaxation factors. The segregated solver uses under-relaxation to control the update of computed variables at each iteration. Default values are generally set by Fluent to meet the demands of the widest range of flow scenarios. Unfortunately, these values did not always provide converged residual values for the models being investigated, so they were changed from their default values of 0.3, 0.7, 1.0, 0.8, 0.8 and 1.0 for pressure, momentum, energy, turbulent kinetic energy, turbulent dissipation rate and viscosity, respectively, to 0.2, 0.5, 0.8, 0.5 and 0.5.

### **4.3 Meshing Techniques**

Initial two-dimensional modeling involved generating a turbine blade profile within GAMBIT. Periodic conditions were imposed along all surfaces in the pitch direction to ensure that conditions seen in the experimental, wind tunnel cascade would be matched. Previous computational work by Hermansson [1999] showed the application of inlet boundary conditions approximately one chord length upstream of the blade and exit conditions 1.5 chord lengths downstream of the blade would not interfere with any flow phenomena within the passage. This trend continued for tip and hub work and is presented in Figure 4.6. The figure displays non-dimensional velocity throughout the passage where the local velocity has been divided by the inlet velocity. Of particular interest is the region upstream of the blade, which remains relatively constant with values around one. This shows the flow to be unaffected one chord upstream of the blade. Notice that as the flow enters the blade cascade there are significant changes in velocity.

After the domain was assembled it was necessary to mesh. Working with a 12X scale on the tip and 11X on the hub model it was possible to use similar mesh sizes and

schemes. For the two-dimensional models, several different mesh sizes were used that resulted in total cell counts of approximately 12,000 and 45,000. These different meshes were employed to investigate the solution variation with mesh size. Each mesh consisted of triangular elements applied with a paving scheme. The variation between two meshes along the tip and hub models is shown in Figure 4.2a-b, respectively. There are minor variations along the suction side of the blade, but other regions seem to agree very well.

While the two-dimensional models were generally easy to mesh and solutions converged in under an hour, the three-dimensional models were generally much more complicated due to geometric entities that included the tip gap, gutter gaps and microcircuits. The small geometric features of these parts required a mesh that was in some cases over an order of magnitude smaller than what was required in the passage thus creating challenging meshing problems.

As discussed in earlier chapters there were four tip geometries and five hub geometries that were explored during the study. The four tip geometries included: a baseline blade consisting solely of a flat tip, a blade containing a dirt purge cavity without coolant flow, a blade with a dirt purge cavity and coolant, and finally a blade containing a dirt purge and microcircuit with coolant. The first two geometries used no coolant flow while the latter two used varying degrees of coolant. The platform geometries included a baseline case with no manufacturing fillet and no coolant, a baseline case with no coolant flow, a geometry with leakage flows and two microcircuit geometries combined with various platform leakage all of which was discussed in great detail within Chapter 3.

Three-dimensional meshing of the tip and hub required the use of multiple volumes due to the large variation in size between such things as the tip gap, gutter and microcircuit when compared to the main passage. As an example of the difficulties that were faced during meshing one should consider that the two tip gaps being studied measured a mere 0.003m and 0.009m, respectively. The entire span of the model measured 0.552m and while only half was modeled, this still presented some difficult meshing challenges. The meshing of the more complicated tip and hub models (those containing microcircuits) will be discussed in detail with the assumption that the simpler models can be deduced with the necessary adjustments in geometry.

The meshing of the three-dimensional model starts with the completion of the geometric construction and assembly. During the building of these models it is critical to take into account the unique geometry and post-processing that will occur after a solution is obtained, as this can significantly influence how a model is put together. Model construction, assembly and meshing requires a trial and error approach that many times needs multiple iterations before a good geometry and mesh can be developed. Generally, the geometry is created from the ground up meaning that points are placed in the model with lines being drawn between points. Faces are made from lines and finally volumes emerge from the assembly of faces. Creating geometry in this manner, as opposed to importing files produced by CAD packages reduces the chance for problems to arise during the translation process. In fact, many files created within a CAD program are not suitable for CFD due in part to the many geometric details that are irrelevant in the computational model.

The microcircuit geometries were originally created using the Unigraphics v18 CAD package with the files exported as iges files for importing into Gambit and the subsequent computational models. Importing the tip microcircuit iges file directly into Gambit produced a file with multiple errors. These errors were only addressed after a third party program, CADFIX, was used to correct many of the problems with the original file. CADFIX created a step203 file that was read into Gambit without any problems with the remaining geometry being built around the tip microcircuit. The platform microcircuit geometries were also exported from Unigraphics as iges files and were imported directly into Gambit without any problems as they were much simpler in nature than those of the tip.

Each face created in the model is individually meshed, followed by the meshing of each respective volume. For the tip models there were up to nine volumes while the hub model consisted of four volumes. The use of multiple volumes ensured a higher quality mesh and was much more advantageous over using one volume by allowing for more control during meshing.

Figures 4.4 and 4.5 provide some information as to the size and location of these volumes within the flow domain. In Figure 4.4 the tip geometry is laid out from top and side views. Notice that within the blade there are volumes for the plenum, microcircuits

and parts of the dirt purge cavity and holes. Outside the blade there is a tip gap volume surrounded by a transitional volume and finally the mainstream passage volume. Each one of these volumes was meshed independently with different size meshes in order to maximize cell placement throughout the model. Similar to Figure 4.4, Figure 4.5 presents the different volumes for the platform model. The four platform volumes consisted of a front volume, aft volume, high passage volume and endwall volume. The endwall volume contained all of the cooling mechanisms (rims, gutter, microcircuits) and was meshed extremely tight when compared to the other three volumes.

Figure 4.7a-d shows some of the grids used around the blade and tip gap region. In Figure 4.7a the meshing around the blade and microcircuit ducts is depicted while Figure 4.7b shows the plenum and dirt purge cavity. In Figures 4.7c-d the microcircuit and blade tip are shown with each of the four images showing the same approximate region along the leading edge of the blade. The following paragraphs will discuss in greater detail some of the meshing in these regions.

For the tip geometry, the tip gap region was of primary concern, thus this region received a higher density of cells than other regions, generally receiving approximately 50-65% of the total cells within the model. The respective volumes consisted of a plenum, two microcircuits, two dirt purge holes, a dirt purge cavity, the tip gap, the main passage and a region surrounding the tip gap. The tip gap contained a minimum of ten hexahedral rows of cells in the spanwise direction with an aspect ratio not to exceed three. This meant that for a tip gap of 0.003m the cells were no larger than 0.0003m by 0.001m. Below the tip gap region and within the blade were several additional volumes that included the dirt purge cavity, two dirt purge holes, the microcircuits and the plenum. The dirt purge cavity and holes were meshed in a manner similar to the tip gap, using a fine hexahedral element (0.001m). Due to the unique geometry of the microcircuit it was necessary to use tetrahedral elements (0.0015m) while the plenum was meshed with coarser tetrahedral elements (0.005m). The main passage was meshed with a coarse tetrahedral mesh (0.010m) with the following two exceptions: the faces around the blade were composed of smaller tetrahedral cells (0.005m) and a separate volume around the tip gap extending down the blade from the tip gap to approximately 15% of the span. This volume, meshed with tetrahedral cells around the tip region, served as a transitional

zone between the extremely tight tip gap mesh and the coarser passage mesh, which in some cases was ten times the size of the smaller mesh.

With the knowledge obtained setting up and meshing the tip model, the platform, while equally complicated, took far less time to complete. The four geometric parts of the platform models consisted of a front passage, aft passage, high passage and endwall volumes. The endwall volume contained all of the cooling mechanisms and was meshed with cells no greater than 0.004m. The gutter gap, measuring a mere 0.001m at its smallest condition was meshed with hexahedral elements (0.0005m) while the microcircuits were meshed with an equally small tetrahedral mesh (0.0015m). With a gutter gap of just 0.001m placing a high density of cells within this region would have lead to a model of enormous size. It was decided that the flow effects within the featherseal were not as critical as those of other entities and thus the meshing around the gutter was not the focus of the work. Instead, the microcircuits and rim leakage were meshed with a higher density of cells as they were considered the main factors in platform cooling based on the coolant mass flowrates. The four plenums were meshed with coarse tetrahedral cells (0.005m) with the remaining passage meshed with coarser cells (0.010m).

#### **4.4 Turbulence and Near Wall Modeling**

Several different turbulence and near wall modeling methods were considered for the simulations performed during this study. Initial two-dimensional models were run with inviscid wall boundary conditions as a baseline to obtain pressure distributions around the blade. Subsequent two-dimensional models were run with a turbulent flow regime, as one would anticipate within a turbine passage. Generally, the variation between models of inviscid and turbulent conditions was fairly small with the only noticeable difference being on the latter half of the suction side of the blade (Figure 4.2a-b). The figure shows various meshes and model types for both tip and platform geometries. One would expect to see little variation between the inviscid and turbulent flows for a high Reynolds number two-dimensional flow since the main passage is not

dominated by viscous forces as the near-wall region is. When modeling microcircuits and film cooling holes, the near wall region is very important to the overall results, meaning the use of an inviscid boundary condition on all walls is not feasible beyond the two-dimensional computations. Thus, all three-dimensional models were run assuming turbulent flow.

All turbulent simulations employed the RNG  $k$ - $\epsilon$  models with non-equilibrium wall functions to model the boundary layer. Past studies by Hermansson [1999] and Radomsky [2000] have shown this method to adequately model secondary flows within a turbine passage. The RNG  $k$ - $\epsilon$  model was derived from the instantaneous Navier-Stokes equations. The analytical derivation results in a model with constants that are different from those used with the standard  $k$ - $\epsilon$  models. Additional terms and functions are also present in the transport equations for  $k$  and  $\epsilon$ .

A RNG  $k$ - $\epsilon$  turbulence model is generally very similar in form to the  $k$ - $\epsilon$  model, with the following refinements:

- (1) the RNG model has an additional term in its  $\epsilon$  equation that significantly improves the accuracy for rapidly strained flows (such as that seen in a blade passage),
- (2) the effect of swirl on turbulence is included in the RNG model, enhancing accuracy for swirling flows,
- (3) the RNG theory provides an analytical formula for turbulent Prandtl numbers, while the standard  $k$ - $\epsilon$  model uses user-specified, constant values and
- (4) while the standard  $k$ - $\epsilon$  model is a high-Reynolds-number model, the RNG theory provides an analytically-derived differential formula for effective viscosity that accounts for low-Reynolds-number effects. Note that effective use of this feature does depend on an appropriate treatment of the near-wall region.

Two approaches are illustrated in Figure 4.8 to deal with the near wall region of a turbulence model, which include the following two basic modeling techniques: wall functions and near-wall modeling. Wall functions do not fully resolve the viscous sub-

layer and buffer layer, leaving semi-empirical formulas to span the viscosity-affected region between the wall and the mainstream turbulent flow while the near-wall model permits the viscosity-affected region to be fully resolved all the way to the wall. Within the figure notice that wall functions maintain a relatively large mesh from the freestream up to the wall when the wall models take over. The near-wall modeling approach involves a very small mesh near the wall that must transition to a larger free stream mesh.

The wall-function approach offers a significant savings in computational resources over near wall modeling by using a collection of formulas and empirical data to approximate laws-of-the-wall for mean velocity and temperature and formulas for near-wall turbulent quantities. There are some instances when wall functions may not always be accurate because of a departure from ideal conditions that include strong body forces, severe pressure gradients which may lead to boundary layer separation, highly three-dimensional effects near the wall, and large blowing and suction around the wall.

Fluent offers two types of wall functions: standard wall functions and non-equilibrium wall functions, both of which require the non-dimensionlized  $y^+$  values of turbulence to be resolved to levels between 30 and 60. The standard wall functions are based on proposals by Launder and Spalding [1974] while the non-equilibrium wall functions offer several modifications to the standard function. Included in these modifications is a log-law that is sensitized to pressure-gradient effects and the two-layer-based concept that computes turbulent kinetic energy in neighboring cells. Generally, non-equilibrium wall functions are considered more robust and accurate than the standard wall function. All computations in this study used non-equilibrium wall functions to approximate the viscous near wall layer.

The other approach to dealing with the near wall region is to develop a two-layer zonal model whereby the viscous boundary layer is resolved all the way to wall without the use of wall functions. Several attempts were made to run a two layer zonal model in which wall  $y^+$  values were resolved to levels approaching one, but the number of cells necessary for this resolution was unachievable for these studies. It was estimated that nearly 10-million cells would be necessary to achieve the necessary resolution. Resolving the turbulent  $y^+$  values to levels at or near one provides an increased near wall modeling capability, but at the high computational cost of significantly more cells.

Computational models using the two-layer zonal modeling are generally meshed with extremely fine cells around all walls to capture the thermal and velocity boundary layers while a coarser mesh is placed outside the boundary layer region.

#### **4.5 Convergence Criteria, Grid Independence and Adaption**

The basic method employed in this study to judge the convergence of a solution involved monitoring the normalized residuals of the continuity, x-, y- and z- momentum, energy, k and  $\varepsilon$  after each iteration. The normalized residuals are calculated by first finding the unscaled residuals. These unscaled residuals are the result of computations that have some numerical errors and as these solutions run through many iterations the numerical errors become smaller and smaller, normally dropping several orders of magnitude. In order to judge convergence it is most convenient to monitor the scaled (normalized) residuals. Taking the largest residual values from the initial iterations and dividing each subsequent residual value by this number will provide a scaled residual. Most models experience significant noise in the residual values during the initial iterations followed by a smooth decaying slope of these quantities.

There is no exact rule for determining when a solution is complete. Fluent has default values of convergence set to  $10^{-3}$  for all quantities except energy, which is set to  $10^{-6}$ . During this study the residuals were required to drop to values of  $10^{-4}$ , with the exception of energy, which was required to reach  $10^{-7}$ . Figure 4.9 shows the scaled residuals of continuity, x-, y-, z- momentum, energy, k and  $\varepsilon$  as the solution progressed to convergence around 850 iterations. Typically, tip cases would require 800-1200 iterations to reach the specified convergence levels while platform cases require 1500-1800 iterations.

To insure solutions did not vary substantially with the various meshes that were used for calculations, grid sensitivity was studied. Obtaining grid independence, also referred to as grid insensitivity, implies that the solution will not vary significantly based on the meshing procedure. As discussed earlier in Section 4.3, a model started with approximately 1-million cells. After reaching convergence, this same geometry could be

meshed again with a coarser or finer mesh (generally finer) and the model re-run. This procedure is normally repeated several times with a comparison of the results from each respective mesh made. The variation in features such as pressure and temperature contours were examined to study grid independence as well as non-dimensionalized pressure and lateral averaged adiabatic effectiveness (discussed in Section 4.6). The comparison of results helped to determine the overall convergence of a solution based on differing meshes. One such example of the variation between three meshes can be seen in Figure 4.10 where laterally averaged adiabatic effectiveness along the blade tip is plotted for three meshes of 1.2, 1.65 and 2.0 million cells. The only variation between each model occurs in a small band when  $x/B_x$  is around 0.075 to 0.20. If there was significant variation between several models additional meshes would be examined to further investigate the cause.

Each flow scenario and geometry was generally meshed in a similar manner to that discussed in Section 4.3 with initial models solving for approximately 1.0-1.4 million cells. Upon obtaining a solution based on residual convergence, the grid was modified to study grid insensitivity. This grid modification can be done very efficiently through the use of what Fluent terms grid adaption. Grid adaption provides the ability to vary the grid based on specified values that are important flow features. Such quantities that can be used for adaption include gradients, volumes, and boundaries.

The study in question involved adaption based on  $y^+$  values, velocity gradients and temperature gradients. This method provided additional cells in areas that were of particular interest and allowed for a more efficient placement of cells when compared to re-meshing the entire model with finer cells. In most cases, models were adapted several times until mesh sizes reach approximately 2-million cells. The primary adaption was based on wall boundary  $y^+$  values. The upper limit of the  $y^+$  values was not to exceed 60 (necessary requirement for accurate wall functions), so that any cell having a value exceeding 60 was modified. Additionally, velocity and temperature gradients were adapted.

Figure 4.11a-c shows cell skewness diagrams for three different cases. For each case the cell equiangle and equivolume skew is presented. The horizontal axis of each plot is a measure of cell quality with zero being a nearly perfect cell and one being a cell

of very poor quality. The vertical axis is a measure of the percentage of cells that fall into each particular category. Notice that in Figure 4.11a, which shows a two-dimensional case the cell quality is excellent, but with the three-dimensional models of Figure 4.11b-c the cell quality drops. Figure 4.11b shows a three-dimensional case with dirt purge blowing while Figure 4.11c shows a case with microcircuit and dirt purge blowing. While the cell quality drops off for both of these cases when compared to the two-dimensional case most cells maintain a quality level less than 0.5.

Figure 4.12a shows a two-dimensional triangular mesh used in the passage of the tip geometry. After applying boundary conditions and obtaining a solution in Fluent the original grid can be modified to more fully capture flow features. In this case the grid was modified by adapting to wall  $y^+$  values that were greater than 60. The results of the adaption are shown in Figure 4.12b. Notice that the region surrounding the blade has been divided into smaller cells to better and more accurately model the near-wall region.

A hanging node adaption method was utilized when modifying the various grids that were used for computations. Grids produced by this method are characterized by nodes on edges and faces that are not vertices of all the cells sharing those edges or faces as shown in Figure 4.13a. The main advantage hanging node adaption offers over such other methods such as conformal adaption is the ability to work with a variety of cell shapes and grid types.

During the adaption process each type of element (tetrahedral, hexahedral) is divided differently. A triangle element is split into four new triangular elements while a quadrilateral experiences a similar split into four parts. A tetrahedral element is split into eight smaller tetrahedra with the division consisting of trimming each corner of the tetrahedron and then subdividing the enclosed octahedron by introducing the shortest diagonal. A hexahedron is split into eight hexahedra while a wedge (prism) is split into eight smaller wedges. Finally, the pyramid cell is split into six pyramids and four tetrahedra. Figure 4.13a-b shows the division of triangular and quadrilateral elements. Accuracy is maintained by not allowing neighboring cells to differ by more than one level of refinement. This prevents the adaption process from over-adapting areas within the domain, ultimately ensuring that the positions of the parent (original) and child (new) cells are similar (reduces errors in flux calculations).

Solutions were solved on one of two UNIX computer systems: the SGI Origin 2100, located in the VT ExCCL computer laboratory and the ICAM SGI Origin 2000, located at the Interdisciplinary Center for Applied Mathematics on the Virginia Tech campus. The Origin 2100 is a four processor machine while the Origin 2000 has 32 processors. Solution times varied substantially based on the mesh size, the number of processors over which the model is spread and the model type (turbulent, laminar, inviscid). Generally, a solution could be obtained within 48 hours when divided over 3-4 processors. Convergence of the scaled residuals needed anywhere from 800-1600 iterations on average with typical tip meshes of 1.6 million cells requiring 1000 iteration while a platform model of comparable size required 1500 iterations.

#### **4.6 Data Analysis**

Computational studies give investigators the ability to examine many flow and heat transfer phenomena that may not be possible to study through experimentation. This study is no exception to that rule. Questions concerning what occurs in areas such as the tip gap, gutter, rim, and microcircuit are extremely difficult if not impossible to examine by an experimentalist. Fortunately, a CFD model that has been benchmarked by experimental data can provide many incites and answers into the underlying physics of a problem. The analysis of data obtained from CFD is critical to explaining the occurrences within a flow. This section details many of the data analysis techniques that will be presented throughout this paper including such things as velocity transformations, in-plane velocity vectors, pitch-wise averaged data, area averaged data and non-dimensional variables.

The flow domain for both the tip and platform was presented in Figure 4.1a-b and again in Figures 4.5 and 4.6. The global coordinate system for each geometry is located with the origin at the stagnation point of the blade, where  $Z$  is out of the page,  $X$  is in the axial direction and  $Y$  is the pitch direction. For tip tests,  $Z$  was zero along the shroud with all spanwise values within the passages negative while  $Z$  was set to zero along the turbine endwall for platform tests with all values in the passage set as positive. Local

coordinates are given as  $x$ ,  $y$  and  $z$ . In most cases,  $x$  distances were non-dimensionlized by the axial chord,  $B_x$ ,  $y$  by the pitch,  $P$ , and  $z$  by the span,  $S$ .

At specified intervals around the blade, planes were created normal to the blade surface and protruding into the turbine passage. These planes, termed SS and PS, referring to their location on either the suction or pressure side of the blade were used to obtain data such as pressure, temperature and velocity throughout the domain. Figure 4.14 depicts the location of these planes along the tip geometry including seven planes on the suction side and six on the pressure side while Figure 4.15 shows the location of eight platform planes. Both Figures 4.14 and 4.15 also have the base point for each respective plane relative to the stagnation location. When extracting data, each plane was specified to have the same number of equally spaced points and consisted of four separate parts: a plane in the main passage along with line rakes at the mid-span, blade-wall and endwall/shroud (depending on the model being a tip or platform geometry) to capture information from the surrounding walls.

To visualize the secondary flow patterns throughout the passage a method was developed by Hermanson and Thole [2000] to plot the velocity data normal to the local streamwise direction as shown in Figure 4.16 and depicted with equations 4-1 through 4-11. Basically, fluid flow at the mid-span is assumed as the reference condition since the mid-span flow is not affected by the shroud or platform region. Variations from this baseline flow path are plotted as secondary flows within the turbine passage. The general methodology employed for this visualization technique involves a transformation from the global  $-X$ ,  $-Y$ ,  $-Z$ ,  $-U$ ,  $-V$ ,  $-W$  system to a local  $-x$ ,  $-y$ ,  $-z$ ,  $-u$ ,  $-v$ ,  $-w$  system. The entire transformation is based on a turning angle of the blade with respect to the global direction  $\theta$ , as the specific measurement plane based on the following equations:

$$x = X \cos \theta + Y \sin \theta \quad (4-1)$$

$$y = -X \sin \theta + Y \cos \theta \quad (4-2)$$

$$z = Z \quad (4-3)$$

$$u = U \cos \theta + V \sin \theta \quad (4-4)$$

$$v = -U \sin \theta + V \cos \theta \quad (4-5)$$

$$w = W \quad (4-6)$$

Theta was calculated from the data points that surround the blade geometry

$$\theta = \tan^{-1} \frac{\Delta X}{\Delta Y} \quad (4-7)$$

The flow angle of the inviscid flow at the midspan was calculated by

$$\Psi_{ms} = \frac{V_{ms}}{u_{ms}} \quad (4-8)$$

After obtaining an angle for  $\Psi_{ms}$ , a translation from the local coordinate system consisting of -x, -y, -z and -u, -v, -w to a coordinate system in the form of a tangential and normal component to the inviscid streamline was necessary. The equations used for this transformation consisted of the following:

$$V_s = u \cos \Psi_{ms} + v \sin \Psi_{ms} \quad (4-9)$$

$$V_n = -u \sin \Psi_{ms} + v \cos \Psi_{ms} \quad (4-10)$$

$$V_z = w \quad (4-11)$$

This concluded the transformation. Plots were then constructed with the components  $V_n$  and  $V_z$  illustrating the off-axis flow phenomena (secondary flows).

In addition to examining the secondary flows within the passage it is also of interest to investigate in-plane velocity vectors. This procedure was used in place of the aforementioned secondary flow technique to look at flows within the tip gap or gutter where there was no inviscid flow direction to use for comparison (required for secondary flows). In particular, two planes were used throughout the analysis of the tip. The first plane passes through the middle of the dirt purge holes and cavity while a second plane is located near the mid-chord of the tip and is oriented normal to the pressure side of blade and dissects a microcircuit hole. In both cases these planes span from the just below the tip gap region to the outer shroud. These particular views are of interest because they show coolant flow leaving the blade and the subsequent interaction with the mainstream and/or tip leakage flow. In-plane velocity is calculated by first finding the orientation angle of the plane as is shown with equation 4-7. Using this angle along with the global velocity components of -U, -V, -W a velocity transformation can be performed with equations 4-4 through 4-6 to obtain local -u, -v, -w components. The components of interest are -u and -w with -v being normal to the plane.

Several non-dimensionalized terms are used within the results section that are of particular interest within the gas turbine community including surface adiabatic effectiveness,  $\eta$ , temperature,  $\theta$ , and pressure,  $C_p$  defined in the following equations:

$$\eta = \frac{T_{aw} - T_{\infty}}{T_c - T_{\infty}} \quad (4-12)$$

$$\Theta = \frac{T - T_{\infty}}{T_c - T_{\infty}} \quad (4-13)$$

$$C_p = \frac{P_{static, local} - P_{static, inlet}}{P_{dynamic, inlet}} \quad (4-14)$$

$$C_{p_{ex}} = \frac{P_{static, local} - P_{static, exit}}{P_{dynamic, exit}} \quad (4-15)$$

Both  $\eta$  and  $\theta$  are measures of temperature. With effectiveness the temperature at the wall is simply a function of the coolant and mainstream flow. This is obtained experimentally by using a wall material of low thermal conductivity while computationally a wall boundary condition is set as adiabatic. For a value of  $\eta=1$ , the wall would have the same temperature as the coolant and we would say the coolant effectiveness is at a maximum. For a value of  $\eta=0$ , based on the definition as defined by equation 4-12, the coolant would have no effect on the wall temperature since it would be the same temperature as the mainstream flow. Simply put, surface adiabatic effectiveness measures the local fluid temperature. When measuring heat transfer within an engine often times the adiabatic wall temperature,  $T_{aw}$ , is used as shown in equation 4.16.

$$q_w'' = h(T_w - T_{aw}) \quad (4-16)$$

Effectiveness is an extremely useful method for determining the capability of an external cooling method and will be presented throughout this report. Experimental work by Couch [2003] has measured  $T_{aw}$  while Christophel [2003] will measure heat transfer coefficients along the blade providing designers with a great deal of information about tip heat transfer.

Non-dimensionalized fluid temperature is presented as  $\Theta$  and similar to adiabatic effectiveness varies from zero to one. A value of zero corresponds to a fluid temperature of the mainstream gas,  $T_{\infty}$ , while a value of one corresponds to the temperature of the

coolant,  $T_c$ . In many cases  $\Theta$  is used to map fluid temperature in flow cross-sections such as the PS and SS planes that were discussed earlier.

Pressure is non-dimensionalized by several equations within this text. All experimental measurements and subsequent calculations of pressure made within the wind tunnel experiments are suited to calculate the pressure coefficient based on inlet conditions as shown in equation 4-14 where the inlet static pressure is subtracted from the local static pressure and divided by inlet dynamic pressure. Some information sent by Pratt and Whitney required exit conditions to be used in the calculation of normalized pressure as seen in equation 4-15.

Each of these non-dimensional numbers is extremely useful and can be easily related to an operating gas turbine engine. While the experimental and computational work takes place near ambient conditions using the non-dimensional values allows for quick comparison. If an adiabatic effectiveness ( $\eta$ ) value was found to be 0.5 in the computations and experimental work done in the Virginia Tech test facility, the temperature of the same engine part could be found by plugging in a few numbers. The only information required to find the comparable engine temperature would be the engine mainstream temperature and coolant gas temperature from which the wall adiabatic temperature of that same engine wall could be found by solving for  $T_{aw}$  in equation 4-12.

An important part of both the experiments and computations is to match as many engine parameters as possible. The pressure distribution is one such variable that is extremely important toward obtaining viable data and while the VT wind tunnel cannot match pressure measurements on a one-to-one basis it is possible to match non-dimensionalized pressure.

Another important technique used for data analysis involves calculating pitchwise-averaged adiabatic effectiveness,  $\bar{\eta}$  which is shown below

$$\bar{\eta} = \frac{1}{L} \int \eta dy \quad (4-17)$$

Particular areas of interest for tip tests consisted of the tip and shroud region while platform tests were primarily concerned with the endwall. To calculate pitchwise-averaged effectiveness all of the respective effectiveness values at each node along a wall were extracted from Fluent and run through a MATLAB program written by Knost

[2002] (Appendix B) where the lateral averaging of effectiveness values occurred. Figure 4.17 depicts the method employed for this exercise. Typically, the program requires the input of two variables. The first variable sets the number of data points,  $n$ , to be taken. Meaning if a value of  $n = 0.05$  was selected, the surface of interest would be divided into twenty vertical regions ( $1/0.05 = 20$ ). The second variable,  $t$ , sets the range around each region from which the data will be taken. If a range of  $t = 0.001$  was chosen, then all data points of effectiveness lying within 0.001 on either side of an original line would be considered to lie within that region and would be used in finding an average effectiveness. For most pitchwise-averaged effectiveness plots the respective first and second variables were set to 0.0125 and 0.002 meaning there were 80 data points with a 0.002 band on either side from which data was included. The process is outlined in Figure 4.17 with two steps. The first step shows the tip domain being divided into  $n$  sections while the second step shows a single band from step one with a range  $t$ , that incorporates all of data points that will be used for the pitchwise-average at that specific location. This method allows the researcher the ability to quantitatively evaluate the averaged effectiveness.

Taking the pitchwise-averaged effectiveness one step further, an area-averaged effectiveness,  $\bar{\eta}$  can be calculated and is shown in equation 4-18.

$$\bar{\eta} = \frac{1}{A} \iint \eta dA \quad (4-18)$$

This method was used for comparing an array of tests and was generally used with the computational data to provide an overall measure of cooling effectiveness with one single number. While not nearly as informative as a contour plot for investigating hot and cool spots along the blade surface it is possible to see some general cooling trends from a wide array of tests using this method.

With all of the computational methodology laid out and presented within this chapter along with a general understanding of the data analysis techniques, the results from both the tip and platform studies will be presented in Chapters 5 and 6. These chapters provide an in-depth look at flow and heat transfer phenomena within a turbine cascade.

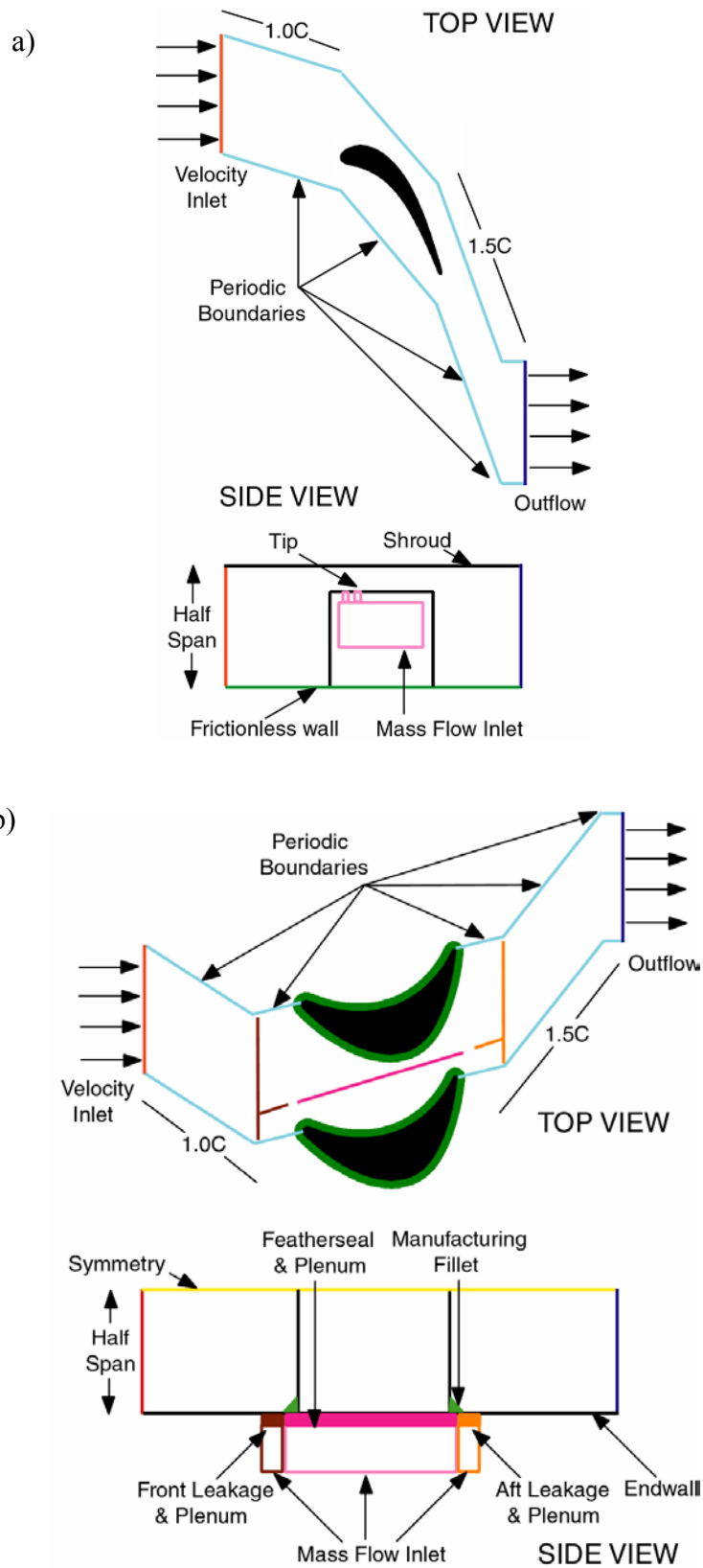


**Figure 4.1a-b.** Boundary conditions placed on the a) tip models and b) platform models.

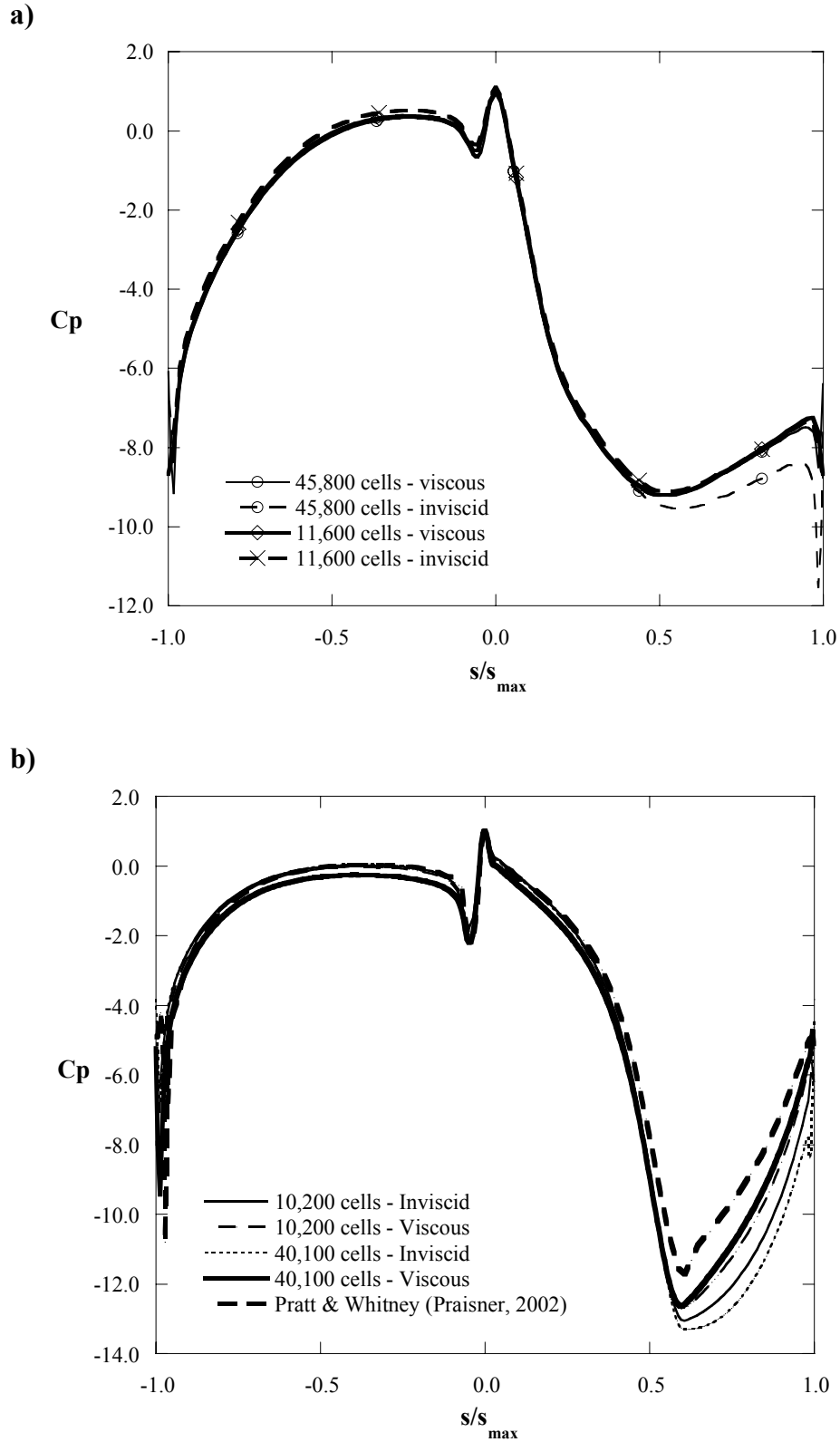


**Figure 4.2a-b.** Comparison of the pressure distributions around the a) tip geometry and b) platform geometry, for a two-dimensional model with various meshes sizes and boundary conditions.

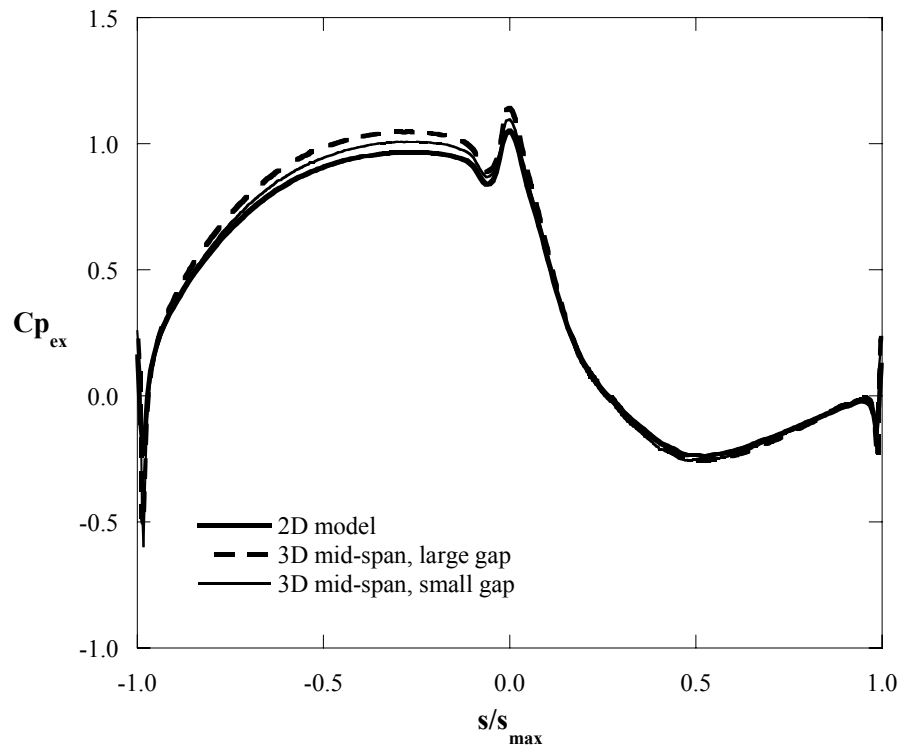


**Figure 4.3.** Pressure distribution for a two-dimensional inviscid model as compared to the pressure distribution at the mid-span for three-dimensional models showing there are no tip gap effects at the mid-span.

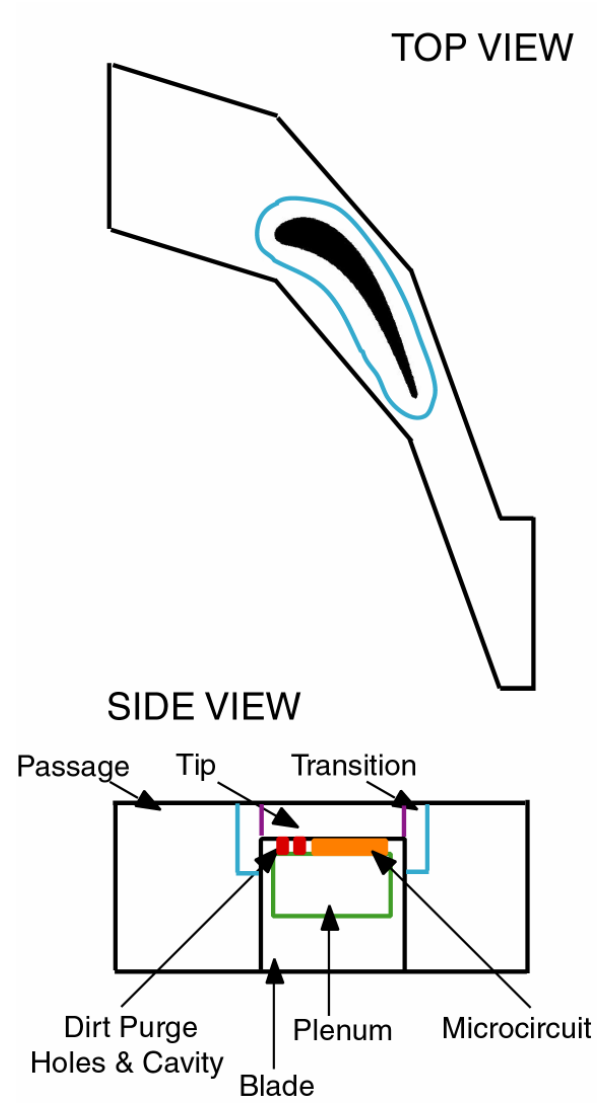


**Figure 4.4.** Depiction of the various volumes that were used for tip meshing including the microcircuits, dirt purge, plenum, transition, tip and passage volumes.

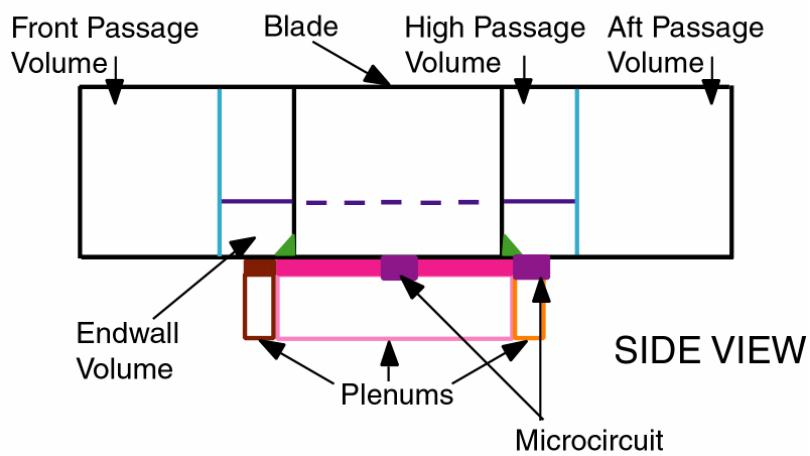
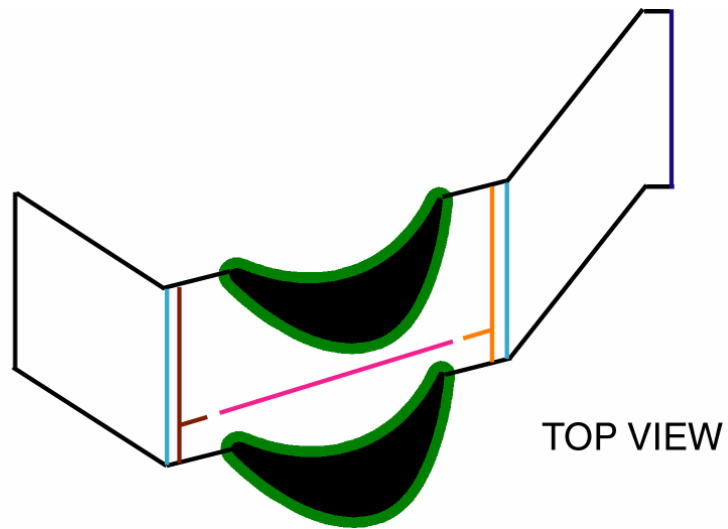


**Figure 4.5.** Depiction of the various volumes that were used for platform meshing including the front passage, aft passage, high passage and endwall volumes.

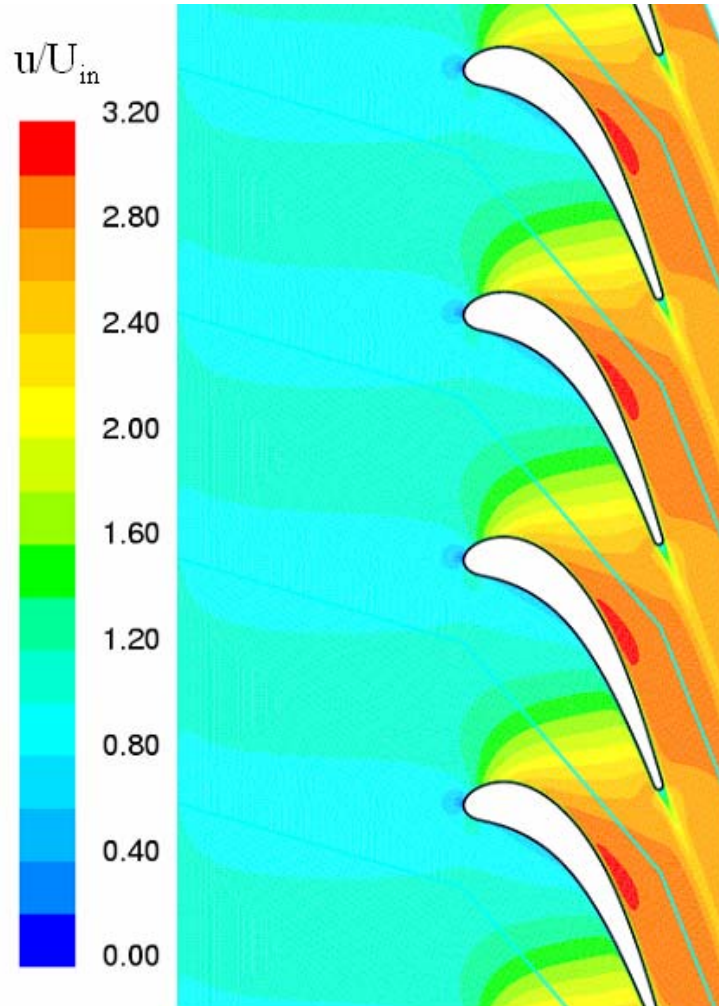


**Figure 4.6.** Contours of velocity magnitude showing the velocity profile is unaffected by the blade one chord length upstream of the stagnation location.

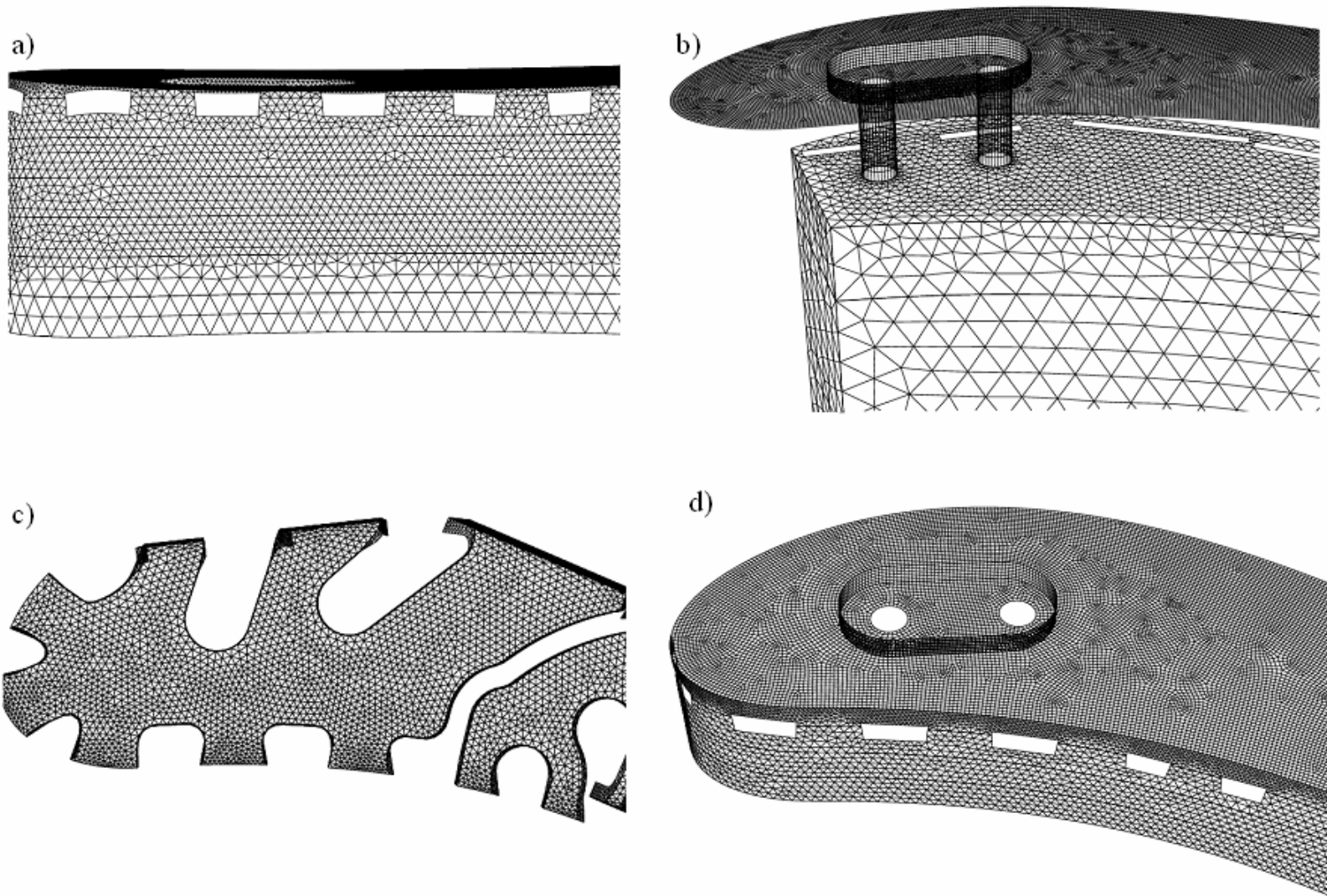


**Figure 4.7 a-d.** Meshing around the a) blade and microcircuit ducts, b) plenum and dirt purge cavity, c) microcircuit, and d) blade tip.

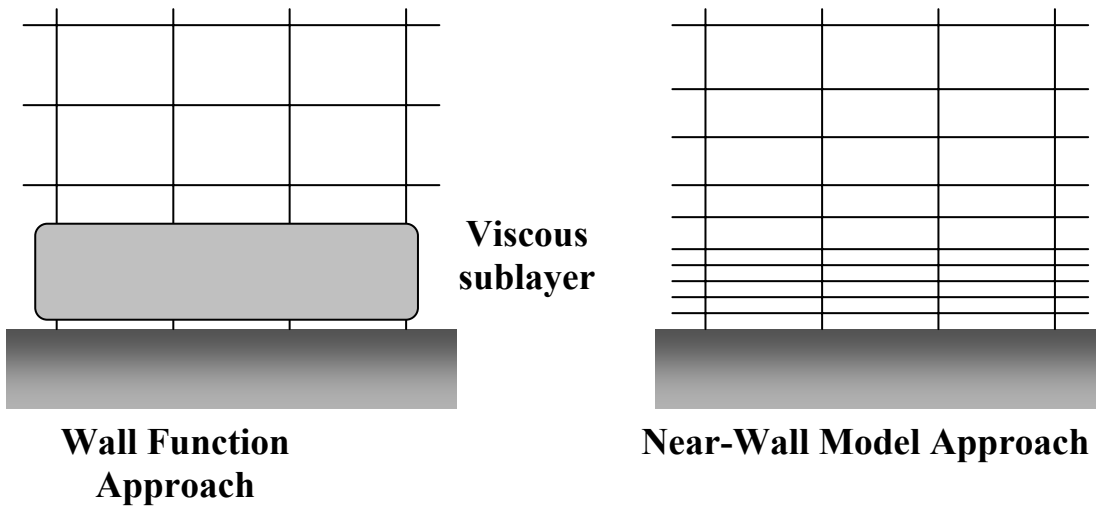


**Figure 4.8.** Two types of boundary layer modeling are possible with Fluent: wall functions and near-wall modeling.

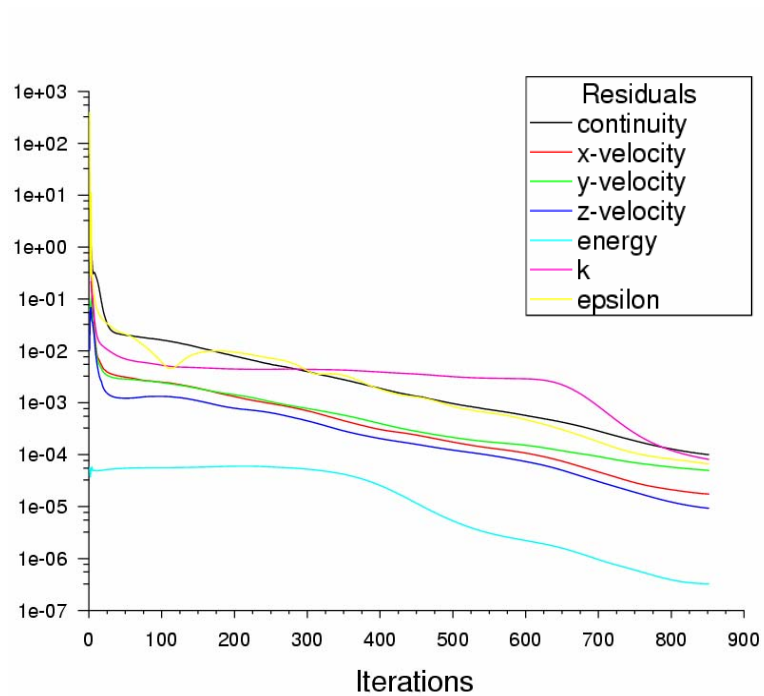


**Figure 4.9.** Typical residual convergence for a tip model.

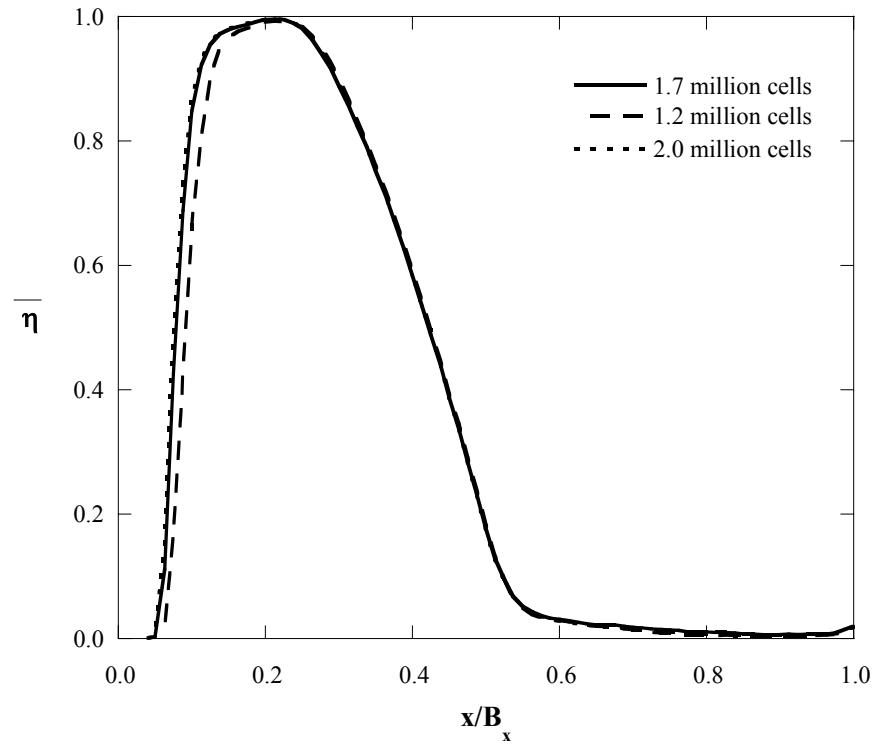


**Figure 4.10.** Laterally averaged adiabatic effectiveness showing the variation between models run with 1.2, 1.65 and 2.0 million cells.

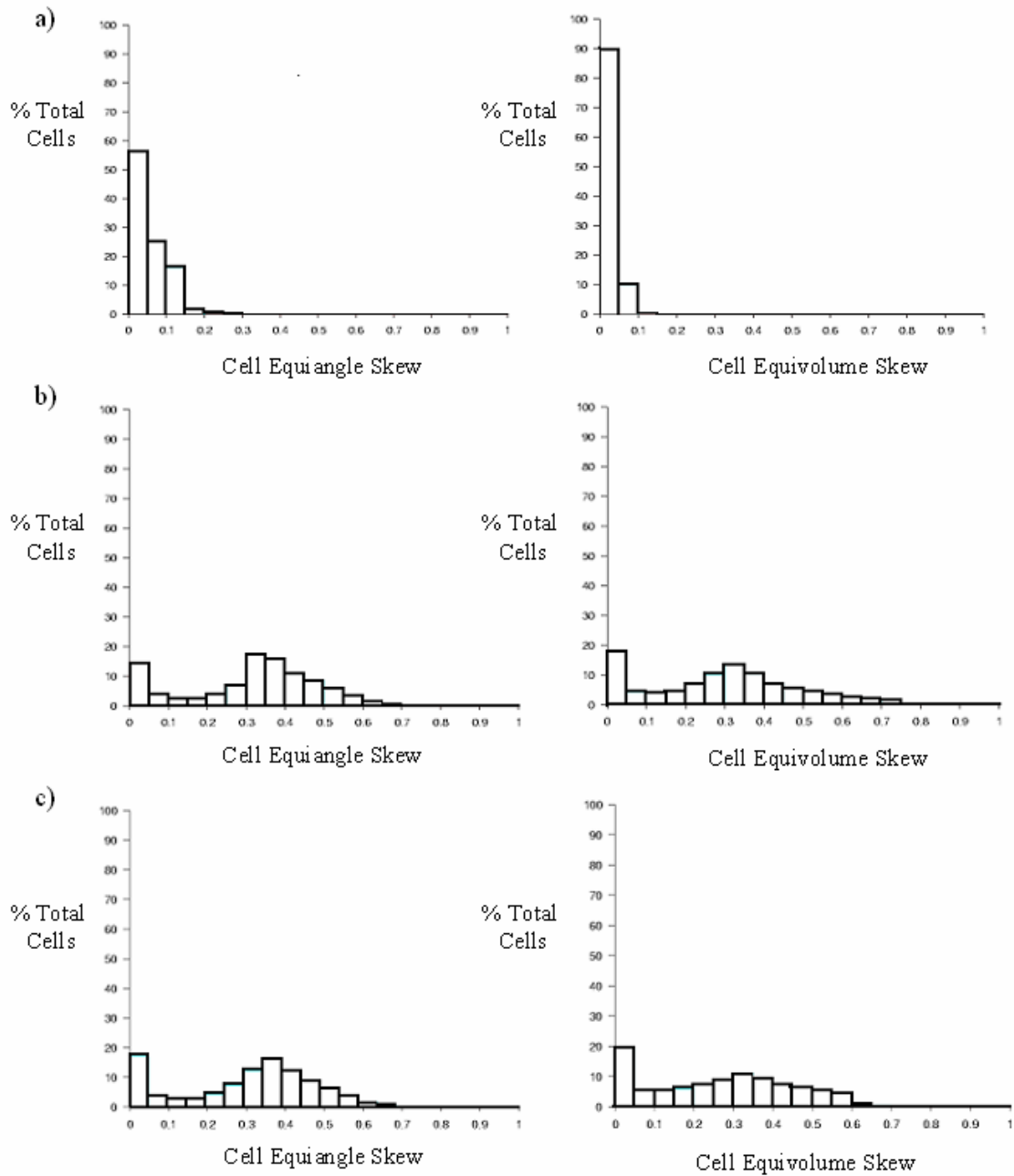


**Figure 4.11a-c.** Cell equiangle and equivolume skewness for a) two-dimensional case, b) three-dimensional case with dirt purge blowing and c) three-dimensional case with microcircuit and dirt purge blowing

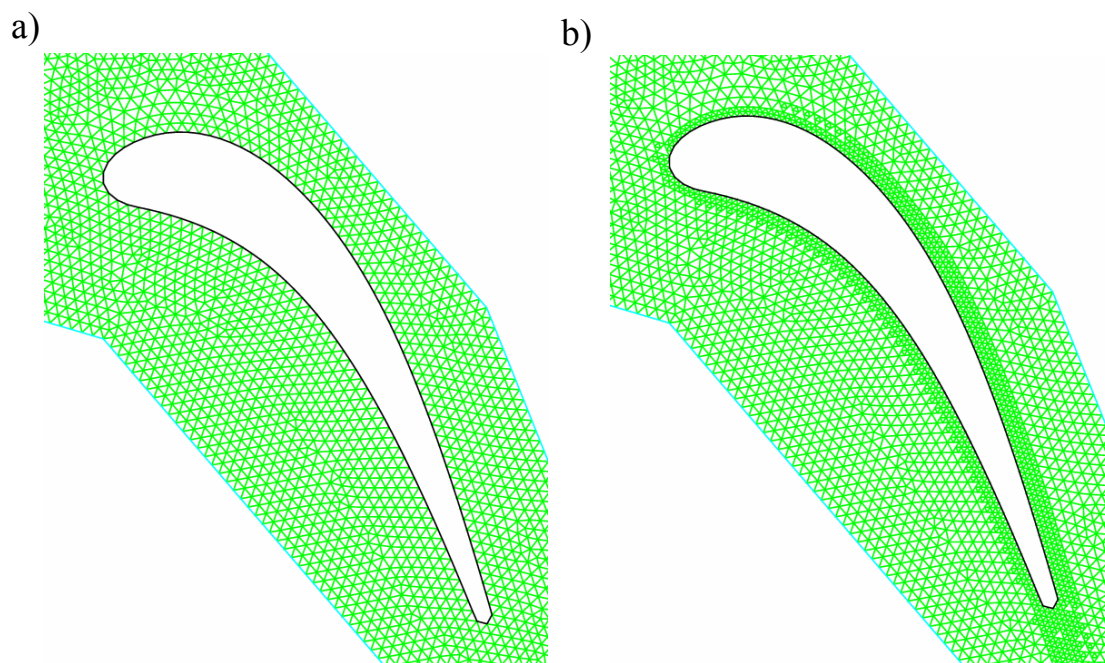


**Figure 4.12a-b.** Two-dimensional tip geometry before and after a grid adaptation, showing the additional cells around the tip surface.

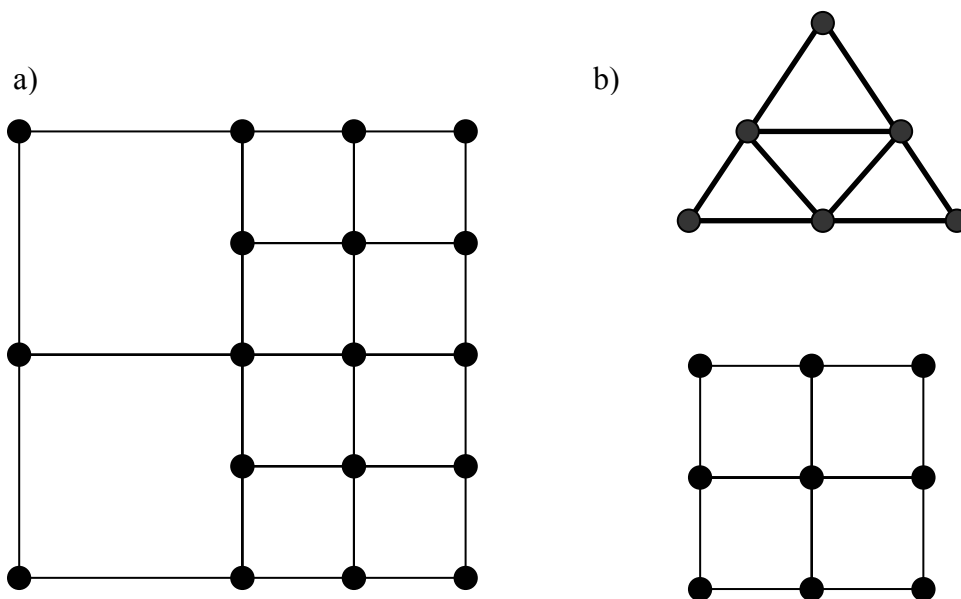


**Figure 4.13a-b.** Meshing procedures employed by Fluent to add additional cells to the flow domain including a) hanging node adaptation and b) the division of triangular and quadrilateral elements.

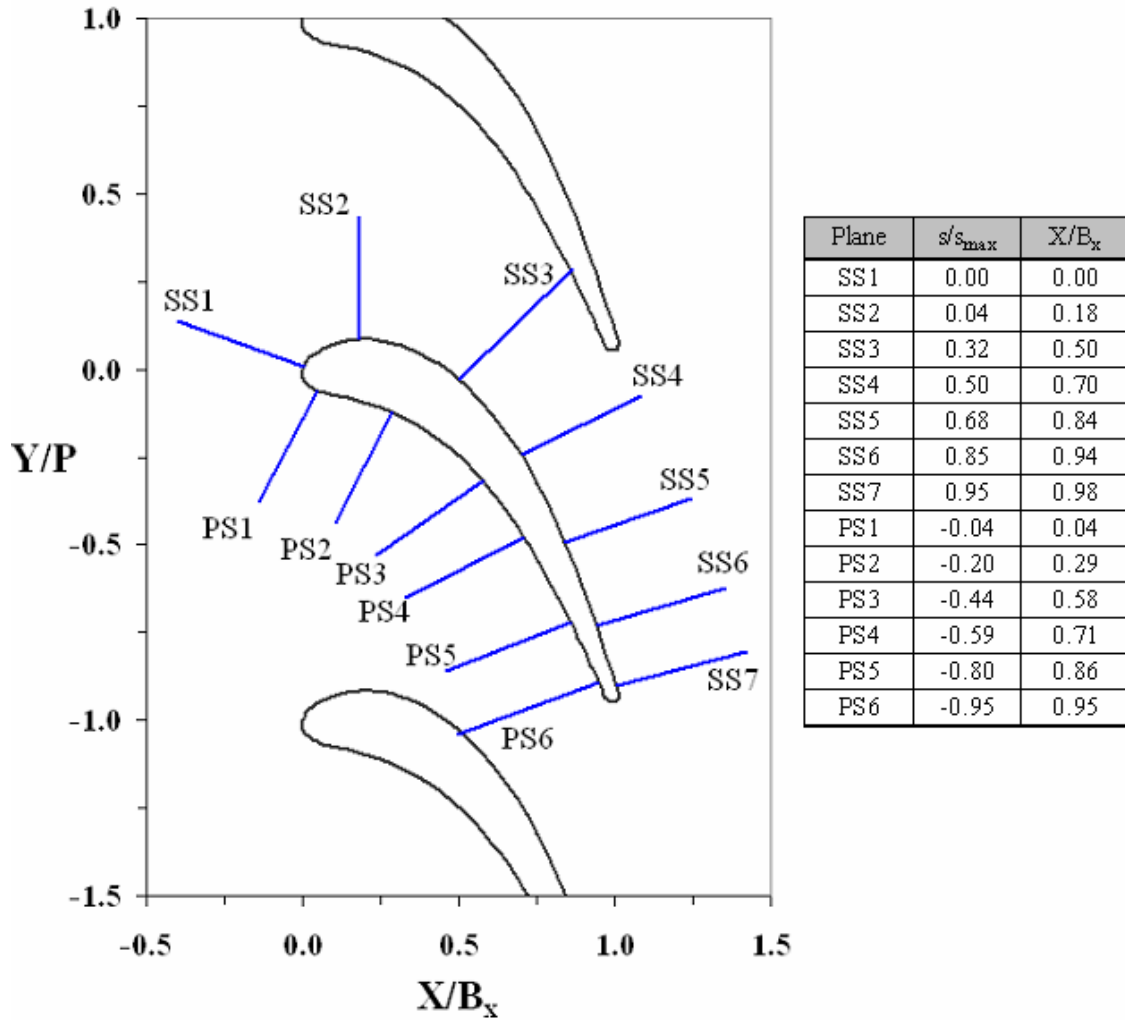


**Figure 4.14.** Location of suction side (SS) and pressure side (PS) data planes relative the position of the blade for the tip geometry.

| Plane | $s/s_{max}$ | $X/B_x$ |
|-------|-------------|---------|
| SS1   | 0.01        | 0.06    |
| SS2   | 0.31        | 0.39    |
| SS3   | 0.68        | 0.88    |
| SS4   | 0.82        | 0.96    |
| SS5   | 0.95        | 0.99    |
| PS1   | -0.15       | 0.07    |
| PS2   | -0.51       | 0.57    |
| PS3   | -0.96       | 0.96    |

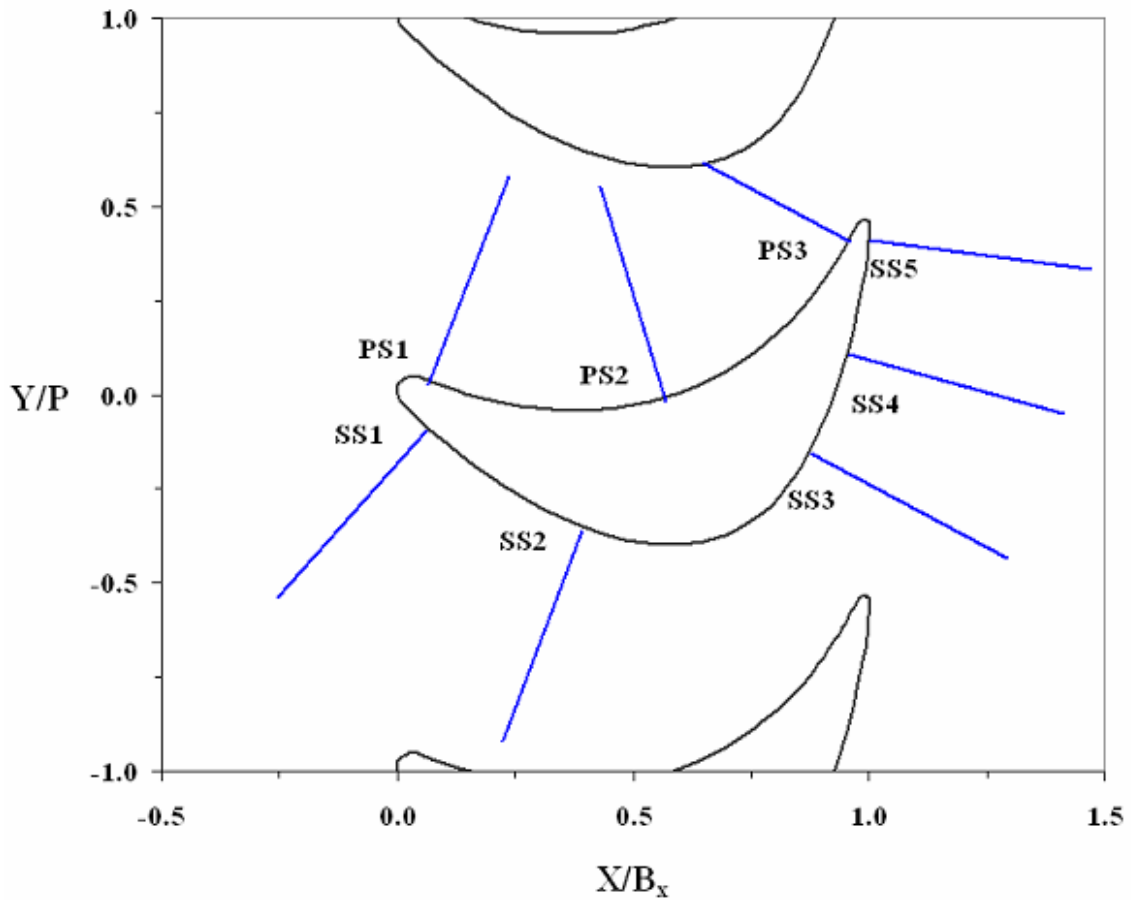


**Figure 4.15.** Location of suction side (SS) and pressure side (PS) data planes relative the position of the blade for the platform geometry.

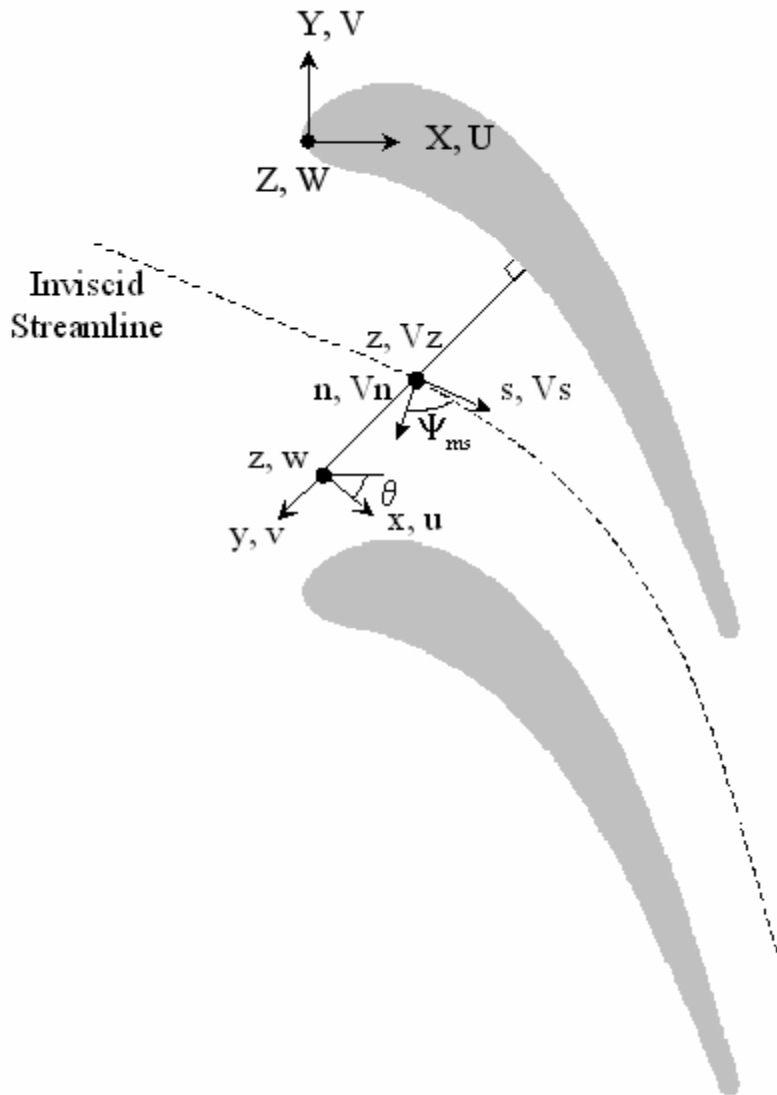


**Figure 4.16.** Velocity transformation process to visualize secondary flows within the flow passage going from global  $X, Y, Z, U, V, W$  coordinates to local streamwise and local normal velocity components.

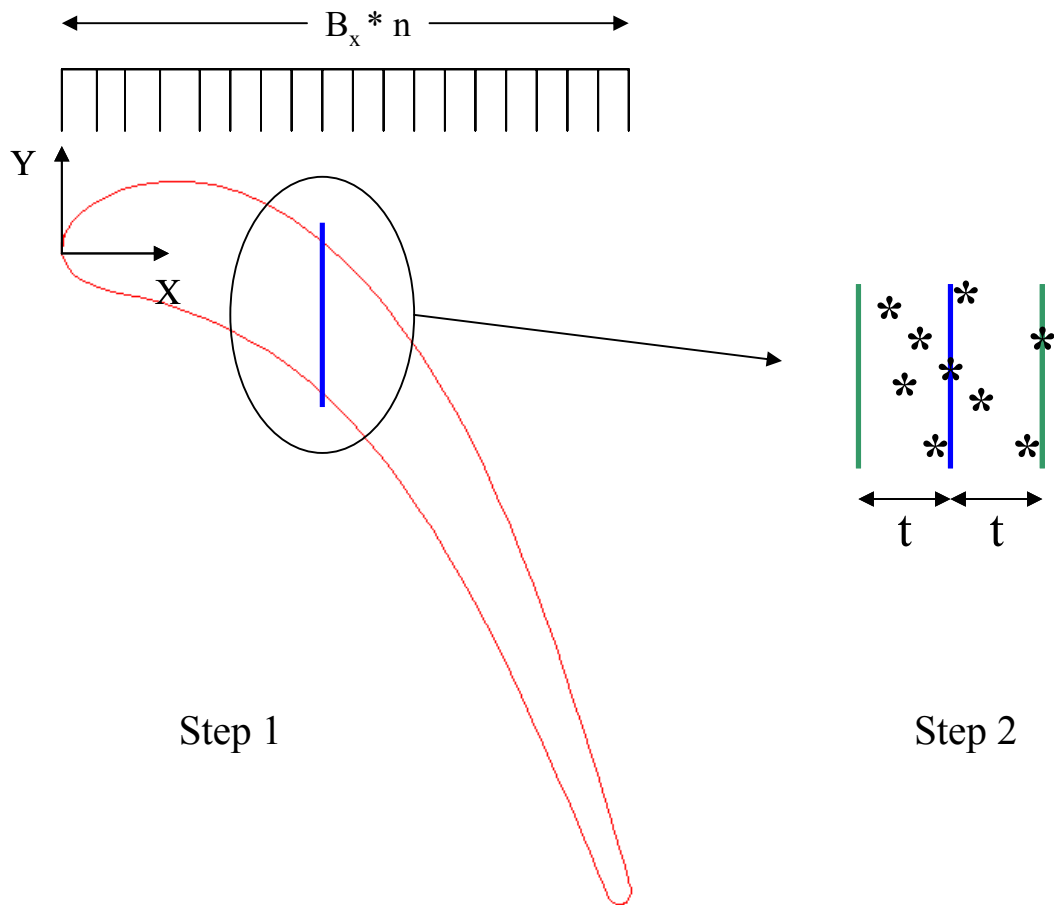


**Figure 4.17.** Process by which data was extracted and laterally averaged effectiveness was calculated. Step 1 shows the division of the domain into multiple sections and Step 2 shows the range of the data points being considered in the averaging process.